

## Simulation of the differential adhesion driven rearrangement of biological cells

James A. Glazier\* and François Graner†

*Research Institute of Electrical Communication, Tohoku University, 2-1-1 Katahira, Sendai 980, Japan*

(Received 7 August 1992)

We show that differential adhesion with fluctuations is sufficient to explain a wide variety of cell rearrangement, by using the extended large- $Q$  Potts model with differential adhesivity to simulate different biological phenomena. Different values of relative surface energies correspond to different biological cases, including complete and partial cell sorting, checkerboard, position reversal, and dispersal. We examine the convergence and temperature dependence of the simulation and distinguish spontaneous, neutral, and activated processes by performing simulations at different temperatures. We discuss the biological and physical implications of our quantitative results.

PACS number(s): 87.10.+e, 75.10.Hk, 64.75.+g, 64.60.Cn

### I. INTRODUCTION

Biological cell shapes and positions rearrange both during morphogenesis and after perturbation of their natural configuration, as in wound healing [1–3]. *In vitro*, spontaneous sorting of two intermingled cell types occurs in aggregates of dissociated cells and yields homogeneous and coherent tissues [4,5]: such sorting is a key step towards reconstruction of functional organs (for a review, see Armstrong [6]). Living organisms [7], even adult animals such as *Hydra*, can regenerate from an aggregate of randomly mixed cells of different types [8,9].

Steinberg suggested that the interaction between two cells involved an adhesion surface energy which varied according to the cell types [10–13]. He interpreted cell sorting via the differential adhesion hypothesis (DAH), which states that cells can ergodically explore various configurations and arrive at the lowest-energy configuration. During the past decades, the DAH has resisted experimental tests better than competing models [6,14]. Recently, Technau and Holstein have obtained experimental evidence that differential adhesion is the main source of cell sorting in hydra cell aggregates [15]. Meanwhile, type-selective surface adhesivity has turned out to be a nearly omnipresent property of cells; in morphogenesis, it is involved in cell recognition [16], gastrulation [17], cell shaping [18], and control of pattern formation [19]; in pathology, it may participate in the migration and invasiveness of cancer metastases [20], and conversely in immunological defenses as well as wound healing [21].

Much literature deals with simulations of cell sorting under the DAH [13]. However, the mechanisms by which differential adhesion can guide cell rearrangement are still unclear. One possibility (*A*) is that cells have an autonomous motility; that is, they move in the appropriate direction using their cytoskeletal apparatus. Motility allows long-range active motion, not to be confused with a second possibility (*F*), namely a simple random fluctuation of the cell surface which allows each cell to locally explore its neighborhood [3,6,22,23]. In practice, it may not be easy to distinguish these two cases experimentally.

A third possibility (*S*) is that even an aggregate made of passive cells could decrease its total adhesion energy and spontaneously relax towards a configuration with the global minimum of energy [24]. Supporting the last two possibilities is the experimental observation that even in the presence of cytochalasin *B*, which prevents pseudopod driven cell motion and membrane ruffling, cell sorting can occur in chick cell aggregates (see Ref. [17] for a discussion) [17,25]. However, this sorting is partial, showing that biological partial cell sorting can occur without fluctuations, but suggesting that some sort of fluctuations are necessary to reach full sorting.

What are the physical implications of this debate? At issue is the texture of the energy surface explored by the cells. The current “active cells” hypothesis (*A*) states that the energy landscape is irrelevant. Even if there are deep local minima in the energy landscape, cells find the global minimum or at least the “ideal” configuration. This is equivalent to assuming that the cell’s exploration of its energy surface is totally ergodic, but also totally dissipative, which apparently requires active cell motion. The fluctuation hypothesis (*F*) acknowledges the presence of only weak local minima, and says that the fluctuation amplitude is large enough to assure diffusion to the global minimum for nonpathological initial conditions. Finally, the diffusionless hypothesis (*S*) states that there are at worst saddle points, with no local minima, and not more than one global minimum of the energy (which might be degenerate, if several configurations are energetically equivalent).

In this paper we survey the energy surface to investigate whether the energy landscape itself provides a coherent description or whether it is necessary to invoke other explanatory mechanisms to account for experimental observations of cell rearrangement. We largely confine our discussion to the behavior of initially randomly mixed aggregates. The formation of such aggregates destroys any preexisting positional signals such as chemical gradients. Thus we examine here the effects of differential adhesion only, separately from chemotaxis, reaction diffusion, active cell motion and cell differentiation. The failure of our simulations to repro-

duce biologically observed effects would give strong evidence that cell rearrangement requires at least the cooperation of a mechanism besides differential adhesion.

The visual similarity between the pattern of bubbles in a soap froth and that of cells in an epithelial tissue was noticed very early [26]. More recently, the analogy between surface tension driven boundary length minimization in a soap froth and biological cells has provided quantitative models for observed cell arrangements [27]. These models are static, explaining the statistics of stable patterns rather than the dynamics of pattern formation. However, the analogy between froth and tissue is a fruitful one, and (since we now understand the basic dynamics of soap froth fairly well) [28] suggests that we could also understand the dynamics of biological tissues, provided that we recognize the intrinsic short-wavelength cutoff implied by each cell's finite size: indeed, each cell has a volume-dependent (or area-dependent, in two-dimensional models) energy term or constitutive relation. Thus we can write a generalized continuous Hamiltonian:

$$\mathcal{H}_{\text{General}} = \int_{\text{cell surface}} j(\tau_{\text{inside}}(s), \tau_{\text{outside}}(s)) ds + \sum_{\text{cells}, i} f_i(a_i), \quad (1)$$

where  $j(\tau_{\text{inside}}(s), \tau_{\text{outside}}(s))$  is the energy of a unit of cell membrane as a function of the membrane type,  $\tau_{\text{inside}}(s)$ , and surface (or medium) with which it is in contact,  $\tau_{\text{outside}}(s)$ ,  $ds$  is a unit of cell membrane at location  $s$ , and  $f_i$  describes the constitutive relation of the cells as a function of their volume  $a_i$ . We assume that  $f_i$  encodes all information concerning bulk cell effects, e.g., membrane elasticity, cytoskeletal properties, etc. In this form, our energy resembles that of magnetic bubbles even more closely than that of soap froth [29]. Thus we explicitly assume that the cell bulk is isotropic, though we have allowed for membrane surface-energy fluctuations within a cell by making the membrane type position dependent.

There are many possible ways to implement such an area-constrained surface-tension Hamiltonian. Since the true system is dissipative rather than conservative, the results of the model depend sensitively on the choice of the dynamics. Possible choices include vertex dynamic, center dynamic, and boundary dynamic models. In this article, we use the extended two-dimensional Potts model which we have presented earlier [30] to simulate various observed cases of cell rearrangement and show how differential adhesion can cause rearrangement without

cell motility. While we are currently extending our simulations to three dimensions, the two-dimensional simulation is sufficient to reproduce the typical types of cell-sorting behavior, including mixing (also known as the checkerboard), complete and partial cell sorting, position reversal and dispersal. We also discuss the convergence of the model, and look in more detail at the quantitative effects of temperature on the simulation to attempt to distinguish thermally activated from spontaneous processes.

## II. THE MODEL

### A. An extended Potts model

#### 1. The Hamiltonian

We use a simple extension of the standard large- $Q$  Potts model [31] to include area constraints and type-dependent boundary energies. We have described the differences in detail elsewhere [30]. Beginning with Eq. (1), we make the additional simplifying assumptions that the surface of each cell is isotropic, i.e., the energy of a unit of cell membrane depends only on the types of the cells on either side [ $\tau(s)=\text{const}$ ], and that the constitutive relation is a simple quadratic elastic term, with all cells of a given type having the same natural volume or area.

The extended Potts model discretizes the continuous cellular pattern onto a lattice, with a spin  $\sigma(i,j)$  defined at each lattice site  $(i,j)$ . In the large- $Q$  limit, we assign a separate spin,  $\sigma \in \{1, \dots, N\}$ , to each of the  $N$  cells in the pattern, with all lattice sites with a given  $\sigma$  composing a cell  $\sigma$ . Thus each cell extends over many lattice sites and need not be simply connected. Typically, each cell in our simulations covers approximately 40 lattice sites, whose spins share the same  $\sigma$ , and we treat approximately  $N=1000$  cells, so  $\sigma$  can assume about 1000 different values.

Each cell also has an associated cell type  $\tau(\sigma)$ , for example, endodermal or ectodermal epithelium. Bonds between like spins have energy 0, that is, the energy inside a cell is zero. Between unlike spins (i.e., at cell boundaries) there is a cell-type-dependent surface energy  $J$ . In addition to their surface energy, biological cells have generally a fixed range of sizes, which we include in the form of an elastic term with elastic constant  $\lambda$ , and a fixed target area, which may depend on cell type. Therefore, our Hamiltonian is

$$\mathcal{H}_{\text{Potts}} = \sum_{(i,j)(i',j') \text{ neighbors}} J(\tau(\sigma(i,j)), \tau(\sigma(i',j')))(1 - \delta_{\sigma(i,j), \sigma(i',j')}) + \lambda \sum_{\text{spins } \sigma} (a(\sigma) - A_{\tau(\sigma)})^2 \Theta(A_{\tau(\sigma)}), \quad (2)$$

where  $\tau(\sigma)$  is the cell type associated with the cell  $\sigma$  and  $J(\tau, \tau')$  is the surface energy between spins of type  $\tau$  and  $\tau'$ ,  $\lambda$  is a Lagrange multiplier specifying the strength of the area constraint,  $a(\sigma)$  is the area of a cell  $\sigma$ ,  $A_\tau$  is the target area for cells of type  $\tau$ , and  $\Theta(x)=\{0, x<0; 1, x\geq 0\}$ . This Hamiltonian is nearly identical to the

lowest-order expansion for the magnetic bubble Hamiltonian [29].

#### 2. Procedure

All our simulations employ a second-nearest-neighbor square lattice. The simulated cells are of two types, low

surface energy or *dark* cells, which we will refer to as *d* cells ( $\tau=d$ ), and high surface energy or *light* cells, which we will refer to as *l* cells ( $\tau=l$ ). In addition, to simulate a fluid medium of unconstrained volume we define an additional cell type ( $\tau=M$ ), and its associated properties, setting its target area  $A_M$  negative, to suppress the area constraint. Thus  $\tau(\sigma)$  can assume three values *l*, *d*, and *M*.

At each time step in the simulation we select a lattice site  $(i,j)$  at random. We convert its spin value  $\sigma(i,j)$  to the spin value  $\sigma'$  of one of the eight neighboring sites, chosen at random, with the following success probability: for temperatures  $T > 0$ ,

$$\begin{aligned} P(\sigma(i,j) \rightarrow \sigma'(i,j)) \\ = \{\exp(-\Delta\mathcal{H}/kT), \Delta\mathcal{H} > 0; 1, \Delta\mathcal{H} \leq 0\}, \quad (3) \end{aligned}$$

and for  $T=0$ :

$$\begin{aligned} P(\sigma(i,j) \rightarrow \sigma'(i,j)) \\ = \{0, \Delta\mathcal{H} > 0; 0.5, \Delta\mathcal{H} = 0; 1, \Delta\mathcal{H} < 0\}, \quad (4) \end{aligned}$$

where  $\Delta\mathcal{H}$  is the gain in pattern energy produced by the change. Suppressing the nucleation of heterogeneous spins is biologically realistic, but we can relax it to allow the nucleation of medium filled vacancies with essentially no change in the results described below. We define one Monte Carlo step (MCS) to be 16 times as many time steps as there are lattice sites. Since we change only one spin at a time and allow it to take only the value of one of its neighbors, the cells move gradually (if granularly) rather than jumping from place to place. We discuss certain pathological nonlocal jumps in Sec. II C 1.

### 3. Surface tensions

It is also useful to define the three surface tensions in the pattern in terms of the bond energies [24]:

$$\begin{aligned} \gamma_{ld} &= J_{ld} - \frac{J_{dd} + J_{ll}}{2}, \\ \gamma_{lm} &= J_{lm} - \frac{J_{ll}}{2}, \\ \gamma_{dm} &= J_{dm} - \frac{J_{dd}}{2}. \end{aligned} \quad (5)$$

These surface tensions  $\gamma$  are not equivalent to a biological membrane's internal tension. The latter appears instead as part of the area constraint  $\lambda$  in Eq. (2). They represent the difference in energy between heterotypic and homotypic interface per unit area of membrane (or per lattice bond). These relative costs do not change if a given constant is added to both  $J_{ii}/2$  and  $J_{ij}$ . We cannot recover our initial surface energies from the surface tensions alone. However, the temperature acts on surface energies, not surface tensions. If we have two sets of surface energies giving the same surface tensions, we expect the final global configuration of the pattern to be approximately the same, but the shape and evolution of each cell can be radically different, crumpled for a low ratio of surface energy to temperature or pinned for a high ratio. If we multiply all the energies by the same positive constant

$C$ , the  $\gamma$  are also multiplied by  $C$  and the evolution remains unchanged only if we multiply the temperature by  $C$ . If we add the same real constant  $c$  to all energies, the surface tensions remain unchanged, but the observed evolution changes unless we also add  $c$  to the energy between two like spins in the same cell, which we usually take as zero for simplicity.

## B. Characteristics of the Potts model

### 1. Advantages

The Potts model has several advantages over other simulation methods. We can easily calculate any desired statistical properties of the pattern and the model runs fairly fast, so we can simulate fairly large aggregates (up to 1000 cells of target area 40 lattice sites) over many MCS's using moderate amounts of computer time.

However, the great advantage of the Potts model is its simplicity. The model is "realistic" in that the position and diffusion of the membrane determine the dynamics, as they do for real loosely aggregated cells. For vertex and center models we must supply the dynamics artificially as a function of fictitious vertices or centers. In the Potts model, relative contact energies and boundary curvatures drive all motion. Thus vertices are always close to their equilibrium condition, and all topological rearrangements happen automatically and rapidly.

We can translate into the language of a vertex model as follows: Since we have defined the self-energy to be zero, the marginal cost of contact area is positive, since all energies must be larger than the self-energy or the model is unstable. The equilibrium contact angles at a vertex are then stable (as in the Young condition), so the cell boundaries "pull" the vertex. If we had defined the energy cost to create new contact area as negative by using negative surface energies, the cell boundaries would "push" the vertex. Whatever mechanism determines the surface energy, it has a lower energy when cell boundaries are paired (e.g., when surface adhesion molecules determine the surface energy, each adhesion molecule has a lower energy when it binds to a corresponding molecule on the surface of another cell, so it attempts to establish new contacts), thus driving the membrane forward, until the local constitutive relations of the cell material and global volume and mass conservation within the whole cell stabilize it.

### 2. Contact angles and topology

In a real moving pattern, the equilibrium contact angle occurs only for slow movement in which the vertices are adiabatically equilibrated. However, whenever a topological rearrangement of the pattern occurs (when two cells come into contact pushing apart two other cells in a *T1* process) the contact angles are wildly out of equilibrium and the boundaries move rapidly until equilibrium is reestablished (Fig. 1). The same holds true for pattern rearrangement after cell disappearance, known as a *T2* process. However, since disappearance normally occurs only in physical patterns which do not conserve cell number

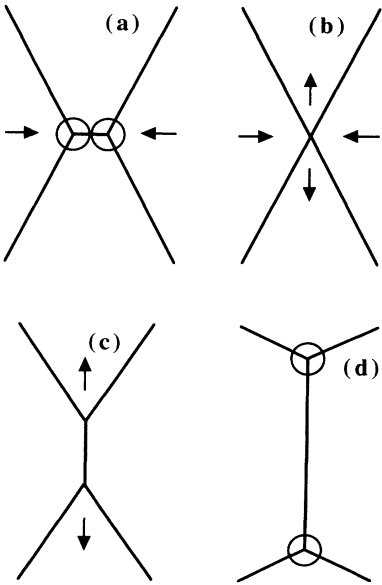


FIG. 1. Topological changes. A  $T1$  process between four equivalent cells. (a) Before the swap all angles are  $120^\circ$ , as indicated by the circles. (b) During the swap there is a single four fold vertex with the angles of  $120^\circ$  and  $60^\circ$ . Note the macroscopic change in equilibrium angle for an infinitesimal movement. (c) After the swap the angles are still far from  $120^\circ$  and the vertices move rapidly. (d) The position of the reequilibrated  $120^\circ$  vertices.

and area, and does not occur in biological patterns, we will neglect it. We define the equilibrium contact angle so that any infinitesimal displacement of the vertex causes a second-order variation of the surface energy, while during a topological rearrangement the energy must vary macroscopically over a small but finite coherence length, typically the rigidity correlation length for biological cells.

In a center model like those based on the Voronoi construction, the coherence length of a cell is comparable to its diameter. Contact angles are given correctly at equilibrium but approach and remain near  $90^\circ$  during a  $T1$  process, since the centers are essentially uninfluenced by topological details like the difference between a fourfold vertex and two neighboring threefold vertices [32,33].

In a vertex model, it is the membrane which adiabatically follows an out-of-equilibrium, slowly relaxing vertex. In such a model the membranes are plane or spherical and vertices have arbitrary angles. In essence, the deviation of the vertex angles from their equilibrium value (for identical cells,  $120^\circ$  in two dimensions and tetrahedral angles in three dimensions) represents the integrated curvature of the cell walls. A pure vertex model with straight walls (e.g., the single-cell-type model of Weliky and Oster) [34] does handle  $T1$  processes correctly. However, for biological tissues, such a model is realistic only for tightly packed cells.

With the extended Potts model we have both features: walls are free to crumple and diffuse, which is not true in

vertex models [34], and contact angles during the  $T1$  process are correct, which is not true in center models.  $T2$  processes occur properly, though they do not normally occur in our simulations since cell area and number are conserved (cell number need not be conserved at very high temperatures or for very weak area constraints). The discretization automatically provides a membrane coherence length of order of a single lattice constant. This coherence length is realistic, but we must consider its implications carefully.

### 3. Limitations

Lattice discretization causes fluctuations in local contact angle, as does lattice anisotropy. The latter also causes boundary pinning. Working at finite temperature  $T$  reduces the pinning but introduces thermal fluctuations in contact angles and boundary shapes [35]. In our simulations we chose  $T$  high enough to avoid pinning of the light-medium interface; however, pinning can occur when dark cells are in contact with the medium (e.g., Fig. 22), since the dark-medium energy is high compared with the temperature.

One physically inspired limitation of the model is that all lattice sites belonging to a given cell are formally identical. The boundaries between cells define the membrane, which has no independent existence, and there is no independent cytoskeleton. We lump all properties of the cell except its surface energy, e.g., its membrane elasticity, its cytoskeletal apparatus, etc., into a single term depending only on cell area. We lump because it allows us to use the Hamiltonian of Eq. (1) and of magnetic bubbles, essentially unchanged, and because we wish to avoid unnatural and *ad hoc* extensions to our model since we do not have sufficient information to describe cell properties in detail.

Thus the model does not distinguish between simply connected and multiply connected cells provided that they have identical areas and perimeters. At zero temperature, for simply connected initial conditions, multiply connected cells never occur. However, when we simulate at nonzero temperatures, surface fluctuations can create multiply connected cells. At low temperatures, the detached cell fragments are small and short lived, and are mainly inconvenient because they disturb our statistical characterization of the pattern. We reduce this problem by annealing at  $T=0$ . We could forbid the nucleation of isolated heterotypic spins, but such rules seem artificial and needlessly complicated, especially since biological cells moving via the extension of lamellipodia often do leave behind small tissue fragments. In addition, we would not (and would not wish to) artificially suppress the necking off of cell segments, which occurs naturally during mitosis. Thus one price of physical simplicity in the model is the presence of multiply connected cells.

Our assumptions also enforce cell isotropy. We cannot create a polarized cell, where membrane elasticity or surface chemistry varies over the cell surface, nor can the cell change shape cytoskeletally. On the other hand, we

understand the physics of this simple model much better than a more complicated and biologically realistic case. Thus we can rigorously distinguish between activated, neutral and spontaneous processes, for example, which would be difficult or impossible for a more realistic model. Since our goal is to determine whether the energy surface created by differential adhesion is *sufficient* to explain a variety of cell rearrangement phenomena, it seems better to start with a model we understand. We discuss possible extensions to improve the model's realism in Sec. IV.

### C. Temperature

#### 1. Statics: Critical temperatures

There are two main critical temperatures in our model. The first critical temperature  $T_{c1}$  is that at which individual cells dissociate. When a spin which is surrounded by only mismatched spins has a long expected lifetime, it can freely detach from the bulk of the cell and the cell falls apart. If we define  $\delta E \equiv J_{ld} - (J_{dd} + J_{ll})/2$ , this dissociation occurs for  $T_{c1}$  of order  $n\delta E$ , where the number of neighbors is  $n=8$  in the next-nearest-neighbor lattice. As we approach this temperature, the constraint that wall lengths are minimized weakens and cell walls can stretch and crumple. In our cell-sorting simulations with  $J_{dd}=2$  for dark cells, dark-dark interfaces have  $T_{dd}=16$  and therefore crumple somewhat, since our usual simulation temperature of  $T=10$  is not very low compared to  $T_{dd}$ . On the other hand, the boundaries between light cells have  $T_{ll}=96$ ; thus they are in their low-temperature limits and their shapes are close to minimal surfaces.

Another effect near  $T_{c1}$  is that the clusters of spins separated from the cell bulk have a longer lifetime than isolated spins and hence can diffuse longer distances. They also have a higher probability to grow to be nearly equal in area to the parent cell, at which point there is no way to distinguish them from the parent. This stable division reveals a nonlocality of the model which is normally hidden, since a spin can then "jump" from one cluster to the other. At low temperatures such large clusters never form spontaneously, and we choose our initial conditions to prevent their occurrence. Near  $T_{c1}$  they can, creating cells consisting of two widely separated nearly equal area masses, which, unlike isolated spins or small clusters, cannot be easily reconnected.

The second critical temperature,  $T_{c2}$ , is that for spinodal decomposition, i.e., demixion of dark and light cells. The spinodal decomposition limit occurs when the entropy and energy are of the same order, i.e.,  $N_{\text{spins}}\delta E = N_{\text{cells}}T_{c2}$ , giving  $T_{c2}=408E=120$  for the parameters we use for cell sorting. Our usual temperature  $T=10$  is much lower than  $T_{c2}$ : thus our simulations are in the low-temperature regime and the lower-energy state corresponds to fully demixed cells.

Here  $T \leq T_{dd} \ll T_{ll} < T_{c2}$ . What happens at higher temperatures? When  $T$  increases above  $T_{dd}$ , the dark cells crumple more until isolated spins detach. These isolated spins easily establish heterotypic contacts. At even higher temperatures, near  $T_{ll}$  the light cells also crumple

then dissociate, and all the spins mix.

In practice, however, these phase transitions occur chiefly for patterns with no free boundaries or for those with very strong area constraints. For the typical parameter ranges which we discuss, increasing the temperature results in the nonconservation of cells, and the pattern loses energy simply by eliminating cells, first light cells and then dark cells. Since the biological limit corresponds to very low temperatures [24], we have not made a detailed investigation of these phase transitions in this paper.

#### 2. Dynamics: Exploring the energy surface

As stated in the Introduction, we want to explore the energy surface and determine whether it contains deep local minima, only weak local minima, or no local minima. Cell motion in these cases requires, respectively, activated, neutral, or spontaneous processes. "Active" biological cells can by definition migrate to the "ideal" final configuration regardless of the energy surface texture. They experience all three types of process with the same rate. On the other hand, passive cells quickly undergo spontaneous transitions, slowly undergo neutral or quasineutral transitions at a rate depending on their fluctuation amplitudes, and cannot escape from deep minima.

We must distinguish the true temperature from the effective fluctuation temperature in biological tissues. Typically, in biological tissues the cytoskeletally driven membrane fluctuations are much larger in amplitude than the true thermal fluctuations, so, for example, when cytochalasin B inhibits cytoskeletal fluctuations, the cell membranes appear essentially fluctuationless [17]. Usually when we refer to temperature in the simulation we are comparing it to the effective fluctuation temperature in tissues.

Varying the simulation temperature allows us to distinguish among these cases. We use it to explore the energy surface, not to simulate its effect on biological systems, since observations always correspond to a low-temperature regime. The rate of spontaneous processes is nearly independent of temperature (or fluctuation amplitude for tissues), since real spontaneous processes, with  $\Delta H < 0$ , have a temperature-independent probability in our Monte Carlo dynamics. In contrast, temperature acts on neutral processes as on diffusion. Finally, some thermally activated processes may depend exponentially on temperature. More precisely, processes which need virtual two-spin flips are exponentially sensitive to temperature, and processes which need virtual  $n$ -spin exchanges to overcome an energy barrier may simply never happen at low temperatures (resulting in a frozen pattern except at high temperatures). In this case, low temperature and zero temperature are equivalent, with the pattern freezing because two-spin processes are forbidden. Note that area conservation essentially requires multispin processes, since a single flip can never conserve cell areas.

#### D. Simulation method

##### 1. Measured quantities

We characterize patterns by their topological distributions, by their boundary lengths, and by the correlations between these quantities, which are all standard measurements for cellular patterns [27]. These are also quantities which can be measured, in principle, in biological experiments. Since the areas of cells are constrained, the distribution of cell areas is generally less informative. Also, we exclude the “cell” defining the medium from our topological calculations. We define the following quantities:  $\rho(n)$ , the probability that a given cell has  $n$  sides; its  $l$ th moments,

$$\mu_l \equiv \sum_{n=1}^{\infty} \rho(n)(n - \langle n \rangle)^l, \quad (6)$$

where  $\langle n \rangle$  is the average number of sides of a cell; the total boundary length, i.e., the total number of mismatched bonds between neighboring lattice sites; and the fractional boundary length, between types  $\tau_1$  and  $\tau_2$ , i.e., the number of mismatched bonds between a spin of type  $\tau_1$  and a spin of type  $\tau_2$  divided by the total number of mismatched bonds. In addition, since the average number of sides of a cell in an ideal infinite cellular pattern with threefold vertices must be six, while the average number of sides of a cell in contact with the medium is five, and of an isolated cell, one, we must distinguish the “total” topology calculated using all the cells from that for “bulk” cells which are not in contact with the medium [36].

##### 2. Annealing

Since we perform our simulation at nonzero temperature, there is no requirement that cells be simply connected. In addition, cell boundaries, especially between low-energy (dark) cells, can crumple if the temperature is comparable to the boundary energy; e.g., in most of the simulations we will discuss,  $J_{ll}=2$ , so the energy of a spin on a light-light boundary is at most 16, comparable to the usual simulation temperature range of  $T=5$  to 10. Since this dispersal and crumpling is a defect of the simulation and is not biologically realistic, we perform a set of zero-temperature annealing steps before characterizing the pattern [35]. To determine how many annealing steps to perform, we ran a zero-temperature annealing on an equilibrated all-light-cell pattern generated at  $T=5$  using  $J_{ll}=2$ ,  $J_{lm}=8$  (yielding  $\gamma_{lm}=7$ ) and  $\lambda=1$ , similar to the one defined below (but unannealed), to ensure consistency with the study of the transient. Since the crumpling and discontinuity of patterns is worse for lower surface energies, this situation is a worst-case limit.

In Fig. 2(a) we show  $\langle n \rangle$  for the bulk and total pattern as a function of time. Note that the value for the total pattern is always less than for the bulk, but follows it closely. We are interested in the degree to which  $\langle n \rangle$  exceeds 6, since this reflects the number of nonsimply connected cells, so we will discuss only the bulk statistics in the remainder of this paper. We begin with the equilibrated initial condition discussed below in Sec. II D 3 and

shown in Fig. 4(b). The initial value of  $\langle n \rangle$  is substantially greater than 6, indicating the presence of numerous disconnected cells. After two annealing steps the bulk  $\langle n \rangle$  has decreased to within 0.2% of its limiting value of  $5.999 \pm 0.004$ , showing that only a few disconnected cells are present (note that on average a cell composed of two sections of roughly equal area will have 10 or 11 sides). The higher bulk moments [Fig. 2(b)] are sensitive to the presence of even one or two disconnected cells. In particular, for about 1000 cells, the change of even a single cell from 11 sides to 10 sides changes the bulk  $\mu_4$  by 0.4, about 40% of its equilibrium value. All three bulk moments decrease rapidly for the first two annealing steps and then very slowly. After two steps  $\mu_2$  is within 9% of its long-time value of  $0.601 \pm 0.006$ , and  $\mu_3$ , which is normally small and positive in our simulations, is within 40% of its long-time value of  $0.0169 \pm 0.006$ .  $\mu_4$  is still 20% above its final value of around  $1.04 \pm 0.01$ , but to bring these values within 3% error we need 20 MCS of annealing. If we look at the total moments including

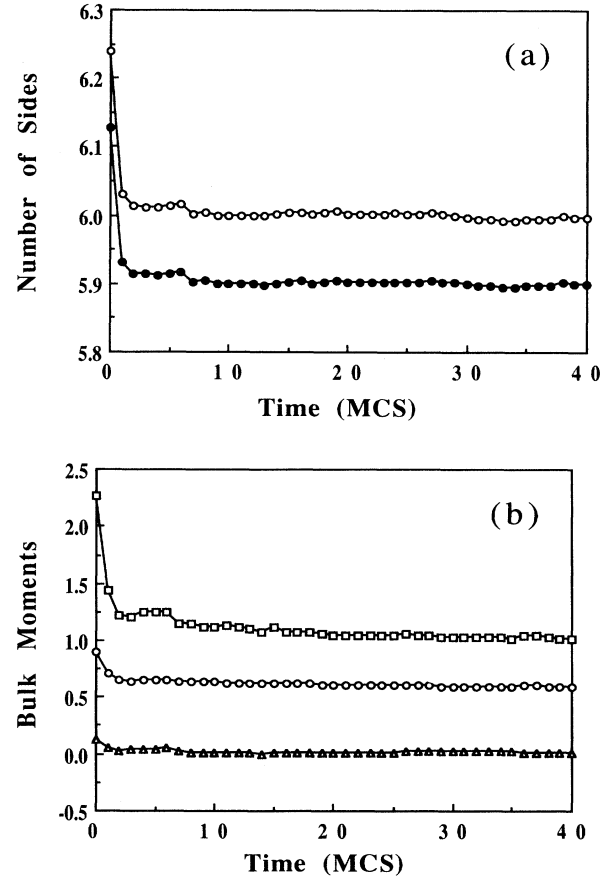


FIG. 2. Annealing. Simulation.  $J_{ll}=2$ ,  $J_{lm}=8$  (yielding  $\gamma_{lm}=7$ ),  $T=0$ , and  $\lambda=1$ . The initial condition is the equilibrated pattern shown in Fig. 4(b). (a) The average number of sides per cell in the bulk (circles) and for the entire aggregate (bullets) as a function of MCS at  $T=0$ . (b) The higher topological moments as a function of MCS:  $\mu_2$  (circles),  $\mu_3$  (triangles),  $\mu_4$  (squares).

edge cells, we find qualitatively identical behavior, since the cell-medium surface has high energy and hence does not crumple.

We can understand this evolution if we look at a detail of the actual pattern. The initial pattern, Fig. 3(a), has crumpled boundaries, with numerous nearby disconnected regions of a few spins. After two annealing steps [Fig. 3(b)], all these defects have disappeared. However, there remain a few grains consisting of two widely separated parts, each of which contains many spins. These take a

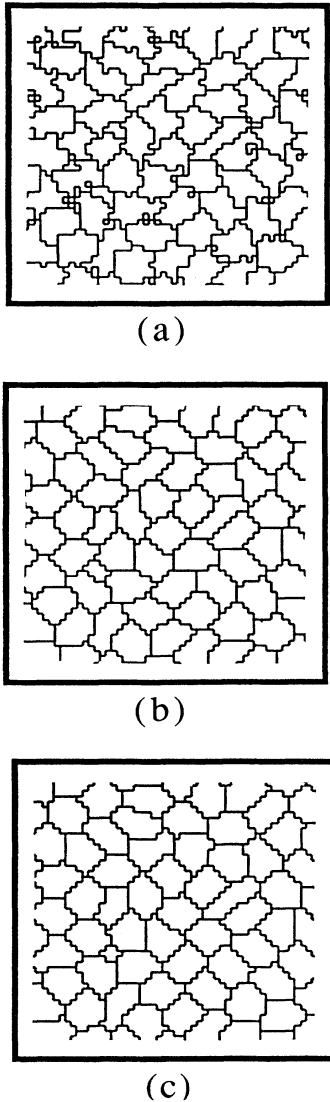


FIG. 3. Annealing. Simulation.  $J_{ll}=2$ ,  $J_{IM}=8$  (yielding  $\gamma_{lm}=7$ ),  $T=0$ , and  $\lambda=1$ . Details of cell boundary evolution during  $T=0$  annealing for the run shown in Fig. 2. Each cell area is constrained to be around 40 spins. We show only cell boundaries, i.e., lattice links between unlike spins. (a) Unannealed. Cell walls are crumpled and there are numerous nearby disconnected spins. (b) After two MCS the walls are compact and there are no few-spin disconnected regions. However, larger disconnected regions persist. (c) Even after 20 MCS a few disconnected regions remain.

very long time to reconnect, hence the slow equilibration of the moments [Fig. 3(c)]. In some cases they can freeze, in which case the pattern will never equilibrate. In the example shown, if we look directly at  $\rho(n)$  we find that there are two persistent disconnected cells with approximately 11 sides. Rather than employing a long and complicated annealing schedule to attempt to eliminate such grains, we prefer to accept them as setting a natural limit of about 10% on the accuracy of our moment calculations, especially since the normal fluctuations of the moments are of this order or larger.

Since annealing also evolves the pattern as well as removing defects, we wish to use as little as possible. We therefore, unless otherwise noted, perform two MCS of  $T=0$  annealing for all displays and statistics. We anneal the displayed data only and do not change the spin array used in the simulation.

### 3. Initial conditions

We have to choose initial conditions with an already equilibrated side distribution. To obtain them, we start

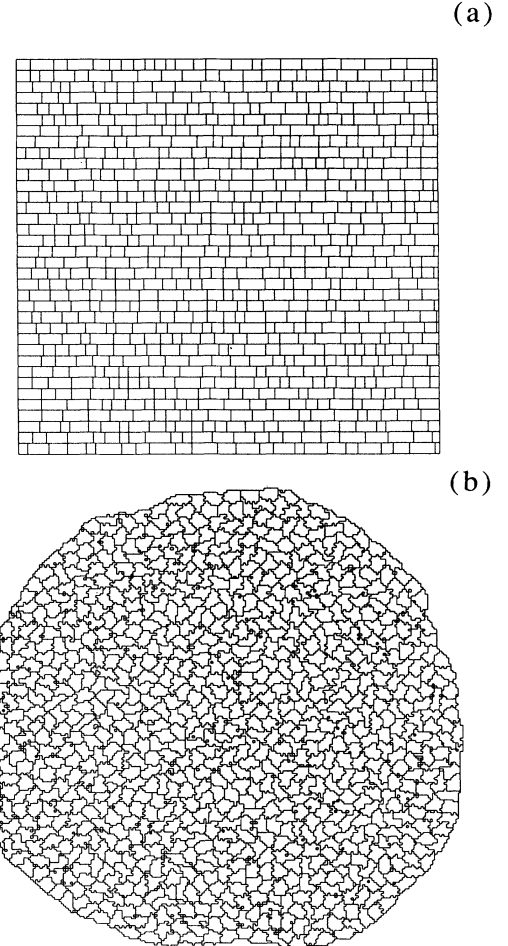


FIG. 4. Global pattern equilibration. Simulation.  $J_{ll}=2$ ,  $J_{IM}=8$  (yielding  $\gamma_{lm}=7$ ),  $T=5$ , and  $\lambda=1$ . (a) Initial rectangular pattern. (b) Rounded pattern after 400 MCS.  $\langle n \rangle = 6.04 \pm 0.01$ ,  $\mu_2 = 0.69 \pm 0.03$ ,  $\mu_3 = 0.03 \pm 0.05$ ,  $\mu_4 = 1.43 \pm 0.12$ . We use this pattern in other simulations as an equilibrated initial condition. Displayed patterns are unannealed.

at first with an arbitrary pattern, here rectangular cells. The equilibration of such a pattern requires both the small-scale breaking of the symmetry of the parallel cell walls and occasional four wall vertices and the large-scale rearrangement of the pattern to eliminate its overall

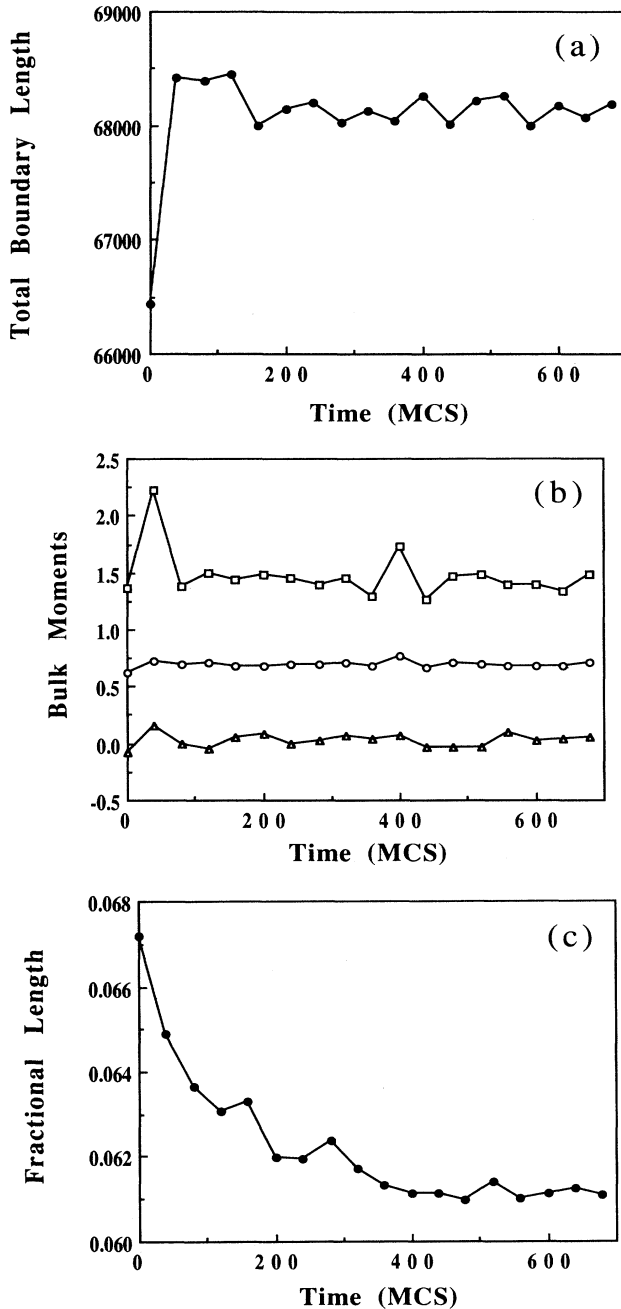


FIG. 5. Global pattern equilibration. Simulation. Statistics for Fig. 4.  $J_{ll}=2$ ,  $J_{IM}=8$  (yielding  $\gamma_{IM}=7$ ),  $T=5$ , and  $\lambda=1$ . (a) Evolution of the total boundary length. (b) Evolution of the bulk topological moments,  $\mu_2$  (circles),  $\mu_3$  (triangles),  $\mu_4$  (squares). (c) Evolution of the light-Medium interface fractional length. Statistics are calculated after ten MCS of  $T=0$  annealing.

square shape. Thus this initial condition tests both large- and small-scale equilibration. We use only one cell type [with  $J_{ll}=2$  and  $J_{IM}=8$  (yielding  $\gamma_{IM}=7$ ), intermediate between future dark and light cells,  $T=5$ ,  $\lambda=1$ ] as we are interested only in the geometry of the walls, not in the rearrangement of dark and light cells.

We show the initial condition in Fig. 4(a) and the pattern after 400 MCS in Fig. 4(b). We calculate all statistics with ten MCS of  $T=0$  annealing; however, both patterns are shown without annealing. In Fig. 4(b) the cell walls are essentially randomly oriented, and the aggregate has rounded into a natural-looking shape, so that none of the original rectangular outline survives. If we look at the total boundary length [Fig. 5(a)], the bulk topological moments [Fig. 5(b)], or the fractional light-Medium boundary length [Fig. 5(c)], we see that they are stable after 400 MCS, the transient being definitely over. The averaged bulk moments are  $\langle n \rangle = 6.04 \pm 0.01$ ,  $\mu_2 = 0.69 \pm 0.03$ ,  $\mu_3 = 0.03 \pm 0.05$ ,  $\mu_4 = 1.43 \pm 0.12$ . We refer to this pattern as equilibrated, and employ it as the initial condition for our other simulations. We then randomly select the cell types, with a seed that we can choose to keep or change. However, we note that while the pattern has no spurious symmetries, it is not necessarily locally equilibrated for different values of surface energy. Therefore we expect a brief (roughly one to five MCS) transient in the topological moments due to local rearrangements to adjust to changes in surface energies.

### III. RESULTS

#### A. Negative surface tension: Checkerboard

##### 1. Observations

Honda, Yamanaka, and Eguchi analyzed the formation of a checkerboard pattern of gland cells (light) and ciliated cells (dark) during the sexual maturation of avian oviduct [37]. We reproduce their experimental images in Fig. 6. The initial state is one in which the two cell types are mixed with significant homotypic contact between irregular shapes [Figs. 6(a) and 6(c)]. However, the distribution of cell types is more homogeneous than a random assignment. During maturation, each ciliated cell divides once, and cells locally rearrange into a checkerboard pattern. Cells become mostly rectangular, with minimal homotypic contact [Figs. 6(b) and 6(d)]. However, the pattern remains far from an ideal checkerboard, since it contains many defects. Note that in both cases the cell areas of the two types are different.

##### 2. Simulations

Honda, Yamanaka, and Eguchi found experimentally that  $J_{ll} - J_{dd} \approx J_{dd} - J_{ld}$ , which corresponds to a negative  $\gamma_{ld}$ . By using the same rough equality to assign our values for the  $J_s$ ,  $J_{ll}=10$ ,  $J_{dd}=8$ ,  $J_{ld}=6$ ,  $J_{IM}=J_{dM}=12$  (yielding  $\gamma_{ld}=-3$ ,  $\gamma_{IM}=7$ ,  $\gamma_{dM}=8$ ),  $T=10$ , and  $\lambda=1$ , we simulate also the formation of a checkerboard, beginning from our equilibrated initial condition with random cell-type assignments [Figs. 7(a)–7(d)].

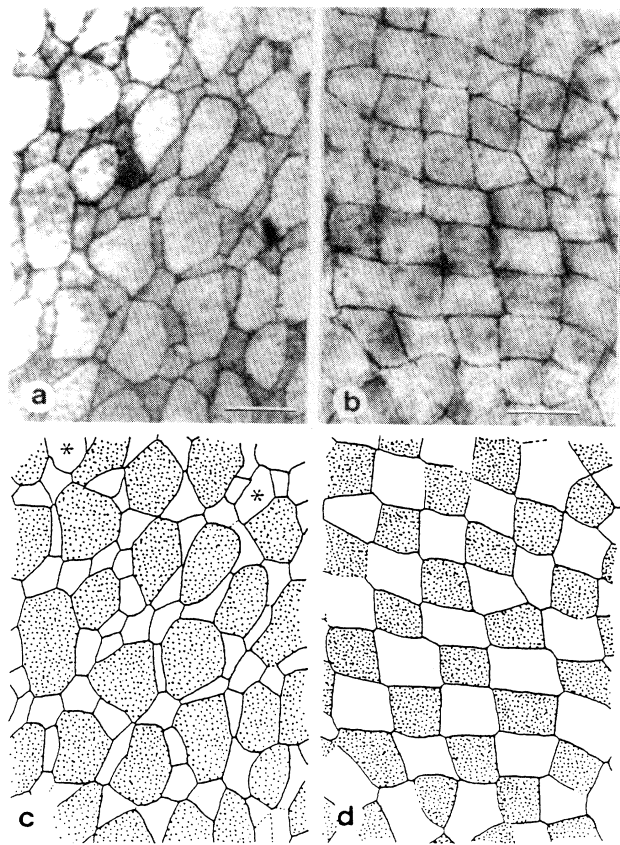


FIG. 6. Checkerboard. Japanese quail oviduct epithelium, photographed by Honda, Yamanaka, and Eguchi, reprinted with permission from H. Honda, H. Yamanaka, and G. Eguchi, J. Embryol. Exp. Morph. **98**, 1 (1986). Copyright Company of Biologists, Ltd., Cambridge, England. (a) and (c) Immature oviduct. (b) and (d) Mature oviduct after the division of each ciliated (dark) cell.

During the first few MCS, small patches of checkerboard appear immediately [Fig. 7(a)], and grow [Fig. 7(b)] till they cover the whole pattern [Fig. 7(c)]. During this period the two cell types rapidly and spontaneously intercalate. As the equilibrated side distribution for a heterotypic aggregate is not the same as for the homotypic aggregate which we employ as our initial condition, we have a transient of roughly 50 MCS during which the total boundary length shortens rapidly [Fig. 8(a)] and the topological moments equilibrate [Figs. 8(c) and 8(d)].

After this initial rapid reorganization, cells continue to diffuse locally. Thus heterotypic cells gradually invade homotypic clusters. The contact length of the two types with the medium remains roughly constant and equal throughout. However, even at long times, many defects remain in the pattern [Fig. 7(d)], since it is difficult for cells to migrate long distances to overcome initial inhomogeneities in the distribution of light and dark cells.

Defect suppression is an activated process, since there are energy barriers to transporting two oppositely charged defects across large regions of perfect checkerboard so that they can meet and annihilate. This activation energy causes large-scale inhomogeneities in the light and dark concentration to persist in the pattern, while local discrepancies disappear. Such incomplete mixing occurs even in the observation of Honda, Yamanaka, and Eguchi [Figs. 6(b) and 6(d)] [37].

The total length decreases monotonically in time, without any sign of saturation during our simulations [Fig. 8(a)]. This apparent logarithmic decrease in boundary length suggests that the pattern is overcoming successively higher energy barriers by thermal activation. If we look at the fractional contact lengths [Fig. 8(b)], we see the heterotypic contact length increase at the expense of homotypic contact length with a gradual saturation. The average number of sides [Fig. 8(c)] and the bulk moments [Fig. 8(d)] are essentially constant after 10 MCS, so the pattern reaches topological equilibrium extremely quickly. We give the averaged moments in Table I.

### 3. Temperature

We can investigate this activated process in more detail by comparing the evolution at different temperatures for identical initial conditions. In Fig. 9(a) we show the light-light homotypic interface lengths and in Fig. 9(b) the light-dark heterotypic interface lengths for a series of different temperatures. The  $T=0$  simulation freezes after about 100 MCS.

For all except the  $T=0$  simulation, the light-Medium interface [Fig. 9(c)] gradually increases at the expense of dark-Medium interface. However, a light monolayer never forms. At long times, the rate of defect suppression, as well as the even averaged bulk moments (Table I), increase with temperature.

The  $T=2$ , 5, and 10 simulations maintain a constant length difference after the first ten MCS. That is, their rate of evolution is the same, indicating that the temperature affects only the initial rapid equilibration and not the subsequent evolution. If we look at the image directly we

TABLE I. Averaged bulk moments of the evolved checkerboard as a function of temperature.  
Statistics are calculated after two MCS of  $T=0$  annealing. Errors are one standard deviation.

$T$	$\langle n \rangle$	$\mu_2$	$\mu_3$	$\mu_4$
0	$6.037 \pm 0.002$	$0.755 \pm 0.002$	$0.078 \pm 0.003$	$1.65 \pm 0.01$
2	$6.04 \pm 0.01$	$0.67 \pm 0.04$	$-0.05 \pm 0.03$	$1.46 \pm 0.12$
5	$6.02 \pm 0.01$	$0.72 \pm 0.04$	$0.05 \pm 0.03$	$1.57 \pm 0.17$
10	$6.06 \pm 0.02$	$0.79 \pm 0.05$	$-0.02 \pm 0.04$	$1.83 \pm 0.25$
15	$6.09 \pm 0.02$	$0.86 \pm 0.04$	$0.07 \pm 0.04$	$2.25 \pm 0.30$
40	$6.25 \pm 0.04$	$1.28 \pm 0.07$	$0.58 \pm 0.26$	$6.68 \pm 1.40$

find that cells in “checkerboard” regions of these low-temperature simulations are effectively frozen.

On the other hand, those in the high-temperature simulations ( $T=15$  and  $40$ ) are able to move freely. In addition, the fraction of the aggregate showing ordered checkerboard decreases at higher temperatures and the interface with the medium fluctuates greatly, producing large concave regions which do not occur at lower temperatures. The light-light homotypic fractional boundary length initially decreases and then levels off [Fig. 9(a)], since the temperature is sufficient to overcome any energy gain due to further boundary length reduction. The light-dark heterotypic interface is exactly complementary in its evolution [Fig. 9(b)], but with the medium the higher interface energies apparently suppress temperature-driven mixing. At  $T=40$  the averaged bulk moments at long times are significantly different from those for all the other temperatures (Table I). The consistency between moments of the low-temperature simu-

lations suggests that these might be useful quantities to measure to seek experimental confirmation of the model.

Thus there are two phase transitions: one near  $T=0$  between a frozen unmixed pattern and a mixed pattern, and a second between a mixed rigid phase and a liquid near  $T=15$ . The second corresponds to a mixing transition, the energy gained by the perfect periodic alternation of dark and light cells being compensated by the thermal fluctuations. Its transition temperature seems dual to the “spinodal decomposition” critical temperature  $T_{c2}$  for cell sorting.

## B. Cell sorting

### 1. Observations

Cell sorting is the classic behavior of mixed heterotypic aggregates. In Fig. 10 we show an experimental observation of Armstrong of cell sorting of neural (light) and pig-

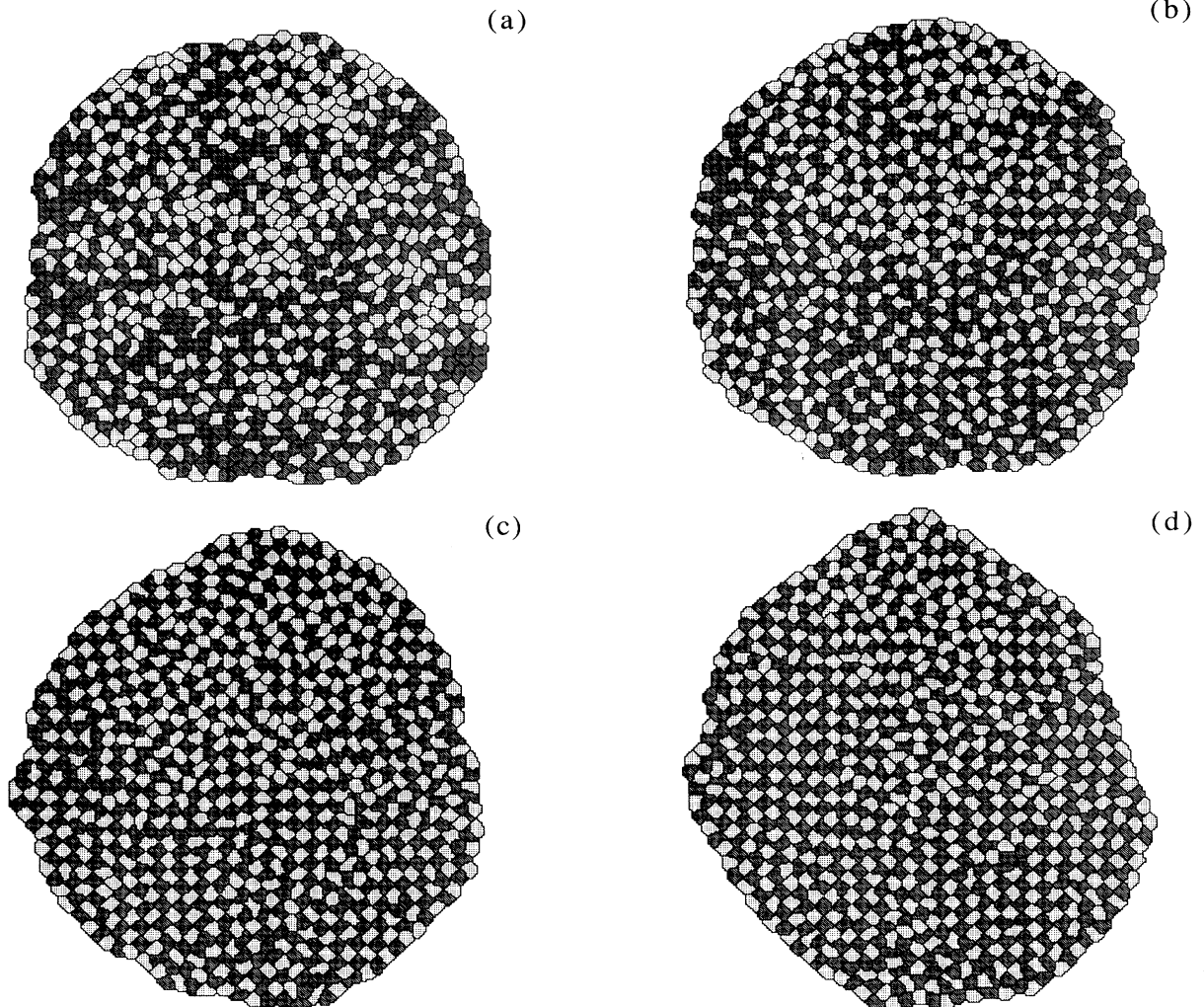


FIG. 7. Checkerboard. Simulation.  $J_{ll}=10$ ,  $J_{dd}=8$ ,  $J_{ld}=6$ ,  $J_{lM}=J_{dM}=12$  (yielding  $\gamma_{ld}=-3$ ,  $\gamma_{lM}=7$ ,  $\gamma_{dM}=8$ ),  $T=10$ , and  $\lambda=1$ , random initial cell type assignment. (a) 10 MCS, (b) 100 MCS, (c) 1000 MCS, (d) 2000 MCS. Patterns are displayed after two MCS of  $T=0$  annealing.

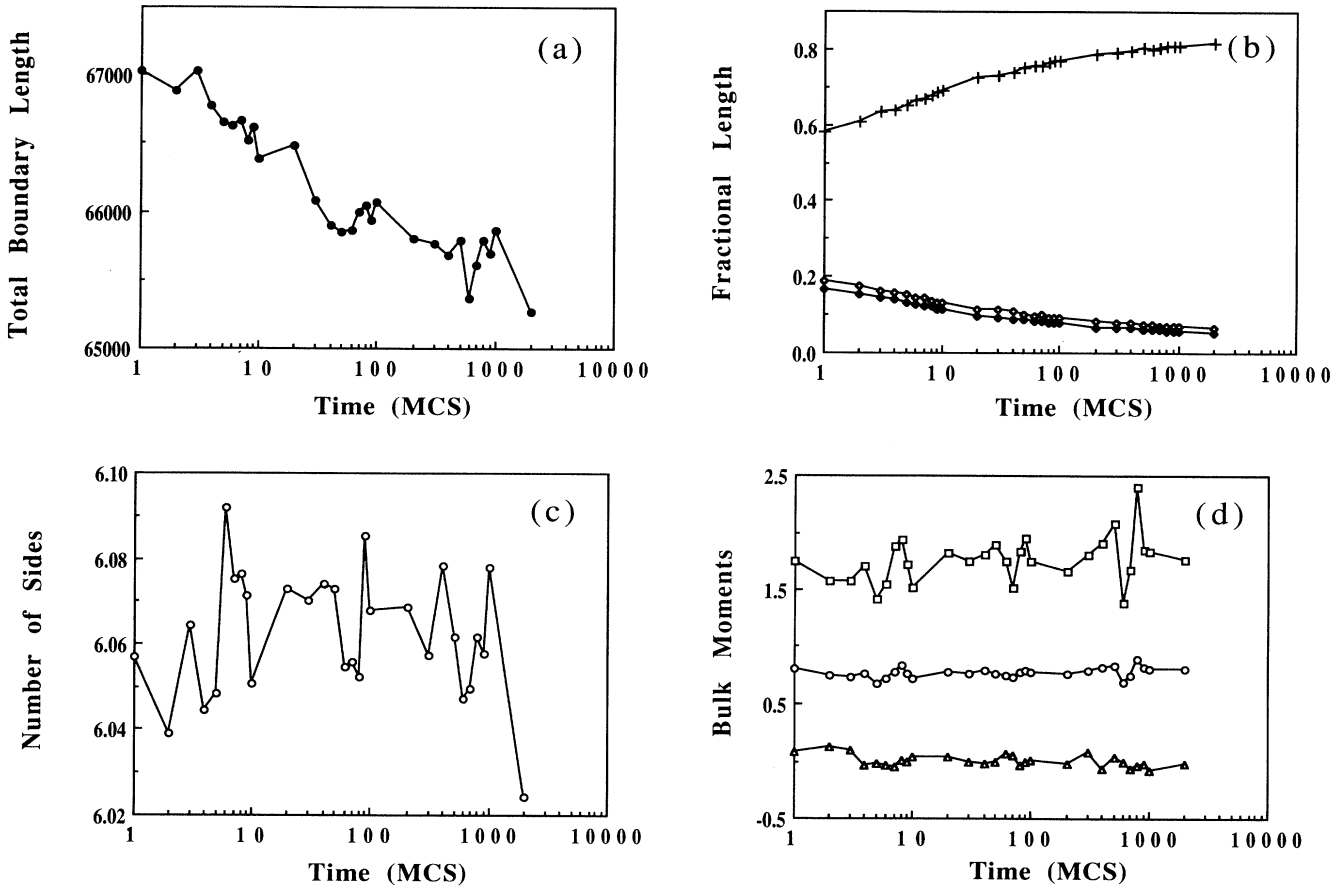


FIG. 8. Checkerboard. Simulation.  $J_{ll} = 10$ ,  $J_{dd} = 8$ ,  $J_{ld} = 6$ ,  $J_{lM} = J_{dM} = 12$  (yielding  $\gamma_{ld} = -3$ ,  $\gamma_{lM} = 7$ ,  $\gamma_{dM} = 8$ ),  $T = 10$ , and  $\lambda = 1$ , random initial cell type assignment. Topological information for the run shown in Fig. 7. (a) Total boundary length. (b) Fractional boundary lengths: light-light homotypic (open diamonds), dark-dark homotypic (solid diamonds), and light-dark heterotypic (crosses). (c)  $\langle n \rangle$ . (d) Topological bulk moments:  $\mu_2$  (circles),  $\mu_3$  (triangles),  $\mu_4$  (squares). Statistics are calculated after two MCS of  $T = 0$  annealing.

mented (dark) retinal cells from chicken embryos [6]. Initially, the dark cells are dispersed throughout the aggregate with some in contact with the medium [Fig. 10(a), after 5 h]. At a later time [Fig. 10(b), after 19 h], they have formed large clusters and are surrounded by a light-cell monolayer. Later still [Fig. 10(c), after 48 h] they form a single rounded mass inside each aggregate which may or may not be well centered.

An identical process occurs, e.g., in mixed aggregates of the slug phase of the slime mold *Dictyostelium discoideum*. We reproduce the observations of Takeuchi, Tasaka, and Kakutani in Fig. 11: (a) early mixed state, (b) initial sorting, (c) light-cell monolayer formation, (d) final sorted state [38,39]. Again, the dark cells are not centered in the aggregate.

In both cases, the light-cell monolayer forms long before the bulk cells sort completely. It is important to remember that all these images show fixed cells, and were taken from several different aggregates. They are not a continuous time series for a single aggregate. In addition, they show two-dimensional sections of an initially three-

dimensional animal. Steinberg, Garrod, and Nicol observed truly two-dimensional cell sorting in confluent monolayers [40].

Technau and Holstein have made a series of direct, nondestructive observations of cell sorting during the regeneration of three-dimensional hydra aggregates. Their method allows them to measure the evolution in time of individual aggregates and to obtain quantitative measurements of the formation of the ectodermal (light cells in our model) monolayer [15]. They find that the initial surface sorting is rapid (about 12 h) and slows apparently logarithmically in time, which is strong evidence against the involvement of any diffusible substance whose effect should increase in time. They have also measured indirectly the relative strengths of the intercellular adhesivities by aggregating dissociated cells in a rotating shaker flask. They find that for hydra epithelial cells, endoderm ( $d$  in our model) is more cohesive than ectoderm ( $l$  in our model). More precisely, their observations imply  $J_{dd} < J_{ld} < J_{ll} < J_{lM}, J_{dM}$ , leaving the relation between  $J_{lM}$  and  $J_{dM}$  undetermined.

## 2. Simulation of phase separation

In our simulations we use the equilibrated pattern discussed in Sec. II D 3 as our initial condition [Fig. 12(a)], with random assignment of cell types. In accordance

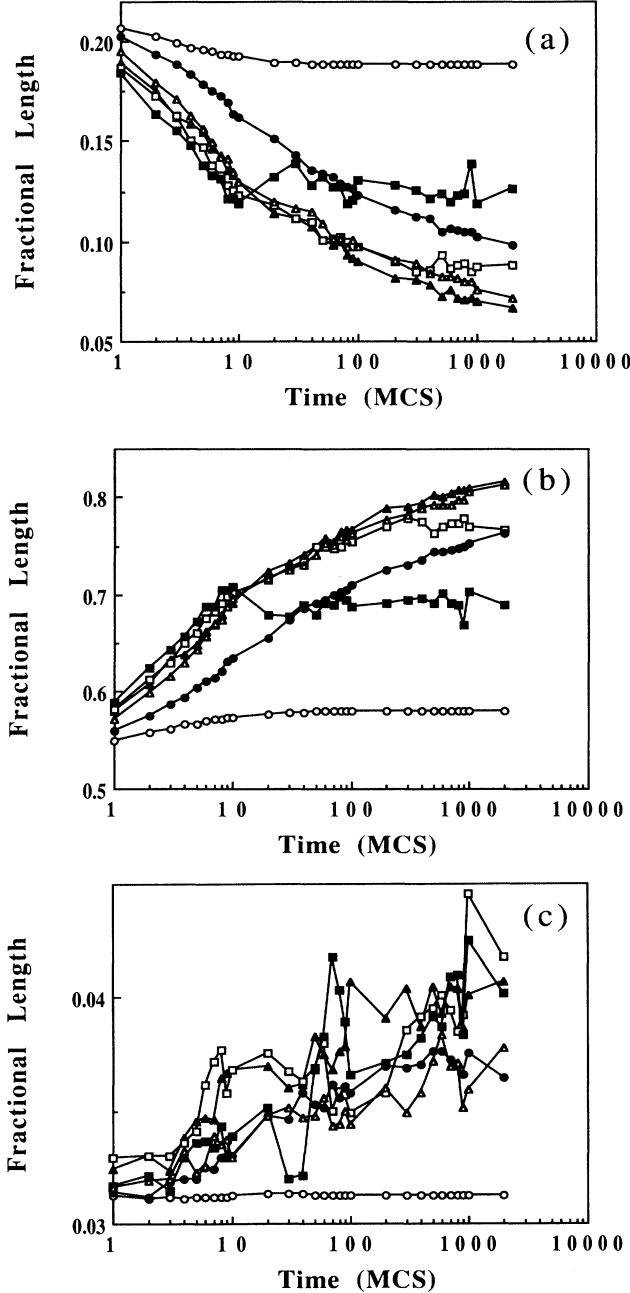


FIG. 9. Checkerboard. Simulation.  $J_{ll} = 10$ ,  $J_{dd} = 8$ ,  $J_{ld} = 6$ ,  $J_{lM} = J_{dM} = 12$  (yielding  $\gamma_{ld} = -3$ ,  $\gamma_{lM} = 7$ ,  $\gamma_{dM} = 8$ ), and  $\lambda = 1$ , identical random initial cell type assignment for each temperature. Comparison of fractional boundary length evolution for different temperatures. (a) Light-light interface. (b) Light-dark interface. (c) Light-Medium interface. Temperatures:  $T = 0$  (open circles),  $T = 2$  (bullets),  $T = 5$  (open triangles),  $T = 10$  (solid triangles),  $T = 15$  (open squares),  $T = 40$  (solid squares). Statistics are calculated after two MCS of  $T = 0$  annealing.

with the observations of Technau and Holstein, the energies are  $J_{ll} = 14$ ,  $J_{dd} = 2$ ,  $J_{ld} = 11$ ,  $J_{lM} = J_{dM} = 16$  (yielding  $\gamma_{ld} = 3$ ,  $\gamma_{lM} = 9$ ,  $\gamma_{dM} = 15$ ),  $T = 10$ , and  $\lambda = 1$ .

The initial sorting into small clusters happens very rapidly over the first few MCS, driven by the large energy difference  $J_{dd} - J_{ld} = 9$  acting on isolated dark cells [Fig. 12(b)]. These clusters then merge, resulting in a slow increase of their average length scale [Fig. 12(c)]. The total

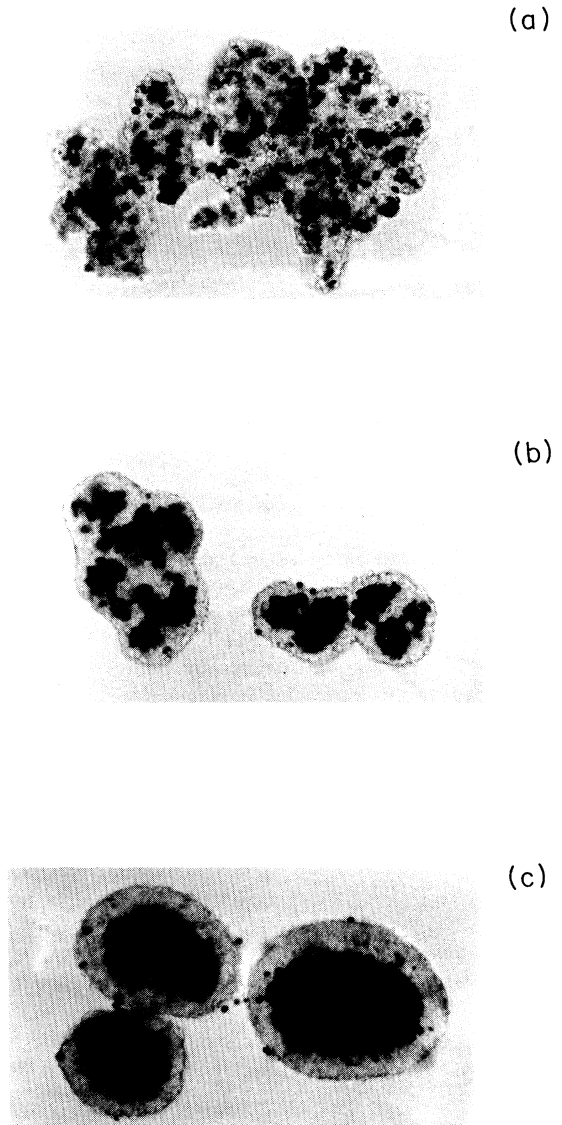


FIG. 10. Cell sorting. Observations by Armstrong of cell sorting between pigmented (dark) and neural (light) retinal cells in seventh-day chick embryo in three-dimensional suspended aggregates. Reprinted with permission from P. Armstrong, Crit. Rev. Biochem. and Mol. Biol. **24**, 119 (1989). Copyright CRC Press, Inc., Boca Raton, FL. (a) Random mixing at 5 h. (b) Partial cell sorting at 19 h. (c) Complete cell sorting at 48 h. Armstrong notes that the detached dark cells in (b) and (c) are dead. Pictures show two-dimensional sections of three-dimensional aggregates.

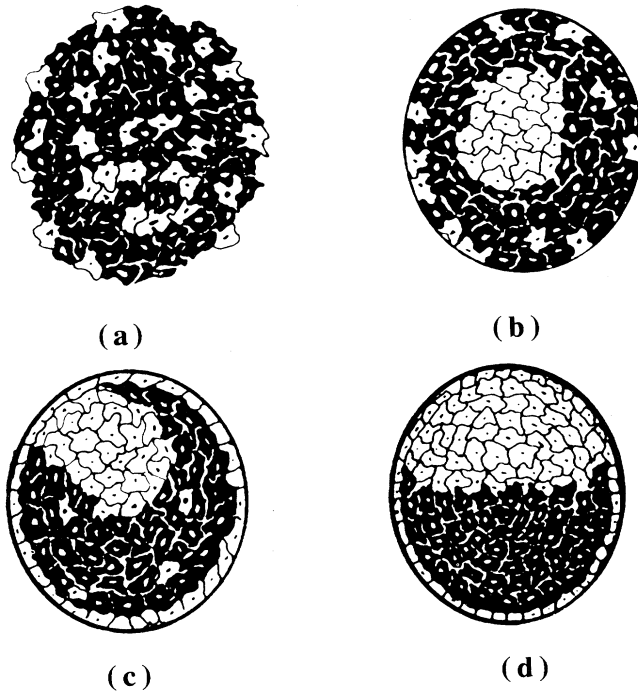


FIG. 11. Cell sorting. Drawing by I. Takeuchi, T. Kakutani and M. Tasaka of cell sorting between prespore (dark) and prestalk (light) *Dictyostelium discoideum* cells in three-dimensional aggregates cultured in roller tubes. (a) Random mixing at 2 h. (b) Partial cell sorting at 4 h. (c) Light-cell monolayer formation at 6 h. (d) Complete cell sorting at 48 h. Pictures show two-dimensional sections of three-dimensional aggregates. Reprinted from I. Takeuchi, T. Kakutani, and M. Tasaka [39] by permission of Wiley-Liss, a division of John Wiley and Sons, Inc. Copyright, John Wiley and Sons, Inc., 1988.

boundary length reaches its equilibrium value by about 100 MCS [Fig. 13(a)]. Similarly, the moments are within one standard deviation of their final values by 200 MCS [Figs. 14(a) and 14(b)], though they appear to increase slightly at very long times, while the correlation functions, which we do not show, exactly mirror the evolution of the boundary lengths. We give the bulk moments in Table II.

The light cells rapidly replace dark cells in the boundary [Fig. 13(b)] due to the energy difference

$J_{dM} - J_{dd} = 14$  versus  $J_{IM} - J_{II} = 2$ . After 600 MCS a monolayer of light cells surrounds the aggregate. The boundary ceases to be a driving force in the evolution [Figs. 12(d)–12(f) and Fig. 13(b)] and the internal rearrangement becomes boundary independent. The time dependence of the surface sorting is very similar to that Technau and Holstein observed in hydra aggregates [15].

Bulk sorting appears in Fig. 13(c). The homotypic boundary rapidly (in about four MCS) replaces the initially dominant heterotypic boundary. The amount of homotypic boundary then increases logarithmically while the heterotypic boundary decreases. The total homotypic boundary of the dark cells dominates, since the light-cell boundary with the medium decreases the amount of light-cell homotypic boundary. We obtain an identical result if we look at the type-type correlation function [Fig. 13(d)].

### 3. Long-time behavior

In Figs. 12(e) and 12(f) we see the reattachment of a large independent cluster of dark cells to the main dark cell mass. In Fig. 12(g), the last isolated light-cell cluster breaks through the surrounding dark-cell mass. This breakthrough appears to be a diffusive process which does not occur at zero temperature. It also depends on  $J_{ld} < J_{II}$ . We will discuss in Sec. III E the biologically observed case of partial cell sorting, in which such breakthroughs cannot occur.

At longer times, the dark cells form a single large cluster surrounded by light cells, which rounds very slowly, being essentially round after 13 500 MCS [Fig. 12(h)]. However, a very slow rearrangement continues with no obvious cutoff. This process is driven over a one-dimensional surface by the small surface tension  $\gamma_{ld} = 3$ , while the cells that need to move form a two-dimensional cluster. In three dimensions, a cluster of  $N$  cells would be driven by  $N^{1/3}$  times more cells, thus we would expect its rearrangement to be much faster. We observe the same crossover at 4000 MCS from logarithmic cluster growth to slow rearrangement if we examine the type-type correlation function [Fig. 13(d)].

Note that even at 13 500 MCS the dark-cell cluster is not centered. There is no first-order energy difference between a round dark-cell cluster centered in the white-cell cluster and one that is off center. There may be an extremely weak second-order effect resulting from the fact that the light-cell boundaries adjacent to the dark cluster and to the interface with the medium are parallel for a

TABLE II. Averaged bulk moments of evolved cell sorting as a function of temperature. Statistics are calculated after two MCS of  $T=0$  annealing. Errors are one standard deviation.

$T$	$\langle n \rangle$	$\mu_2$	$\mu_3$	$\mu_4$
2	$5.994 \pm 0.004$	$0.48 \pm 0.04$	$-0.04 \pm 0.02$	$0.74 \pm 0.14$
5	$6.02 \pm 0.01$	$0.50 \pm 0.04$	$0.01 \pm 0.03$	$0.88 \pm 0.11$
10	$6.12 \pm 0.02$	$0.77 \pm 0.05$	$0.32 \pm 0.15$	$2.47 \pm 0.55$
15	$6.30 \pm 0.04$	$1.18 \pm 0.09$	$1.04 \pm 0.30$	$6.71 \pm 1.69$
20	$6.50 \pm 0.06$	$1.64 \pm 0.15$	$2.14 \pm 0.61$	$13.84 \pm 3.72$
40	$6.82 \pm 0.09$	$2.52 \pm 0.21$	$4.45 \pm 0.83$	$32.42 \pm 7.80$

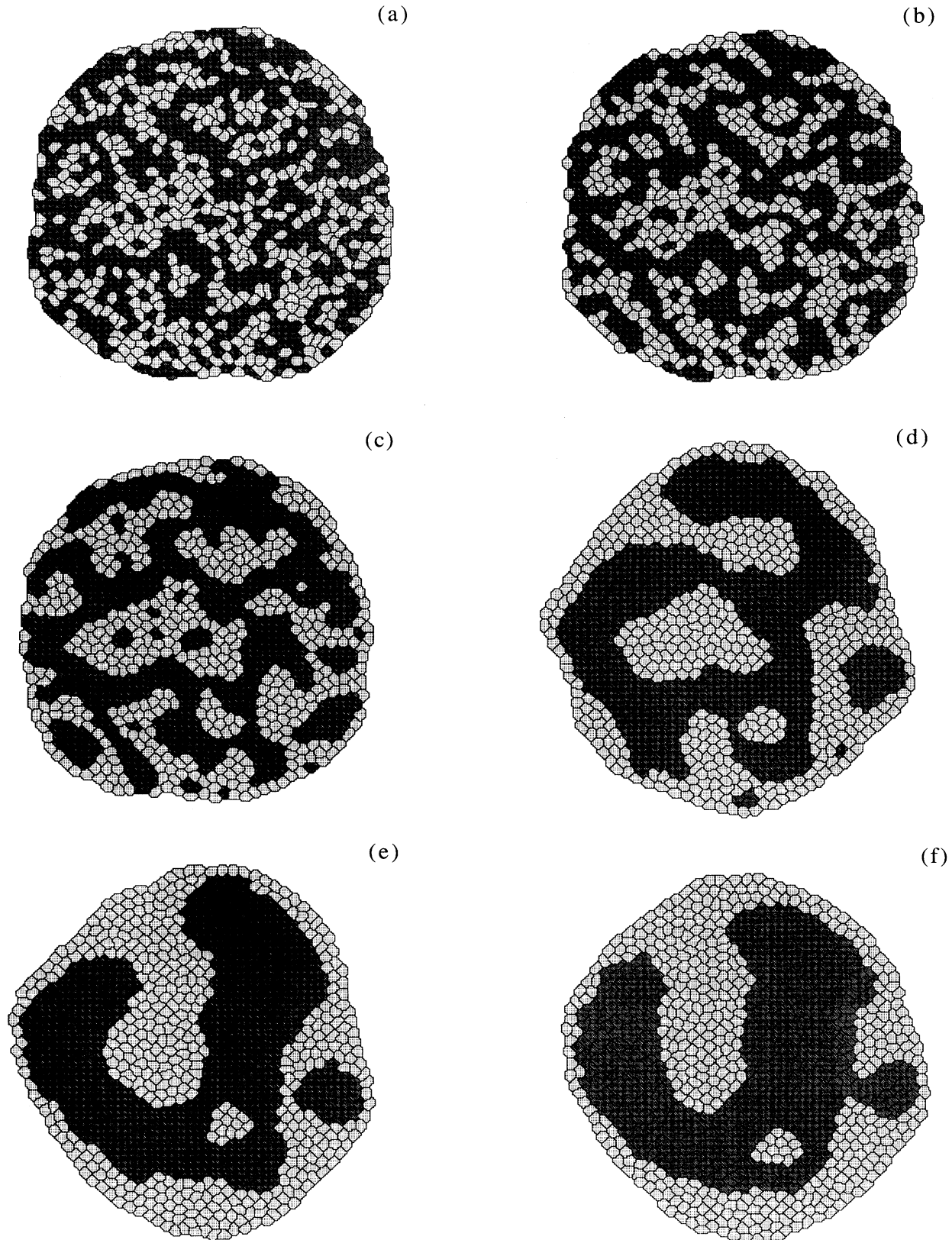


FIG. 12. Cell sorting. Simulation.  $J_{II} = 14$ ,  $J_{dd} = 2$ ,  $J_{Id} = 11$ ,  $J_{IM} = J_{dM} = 16$  (yielding  $\gamma_{Id} = 3$ ,  $\gamma_{IM} = 9$ ,  $\gamma_{dM} = 15$ ),  $T = 10$ , and  $\lambda = 1$ , random initial cell type assignment. (a) 0 MCS. (b) 10 MCS. (c) 100 MCS. (d) 1000 MCS. (e) 3000 MCS. (f) 4000 MCS. (g) 5000 MCS. (h) 13 500 MCS. Patterns are displayed after two MCS of  $T = 0$  annealing.

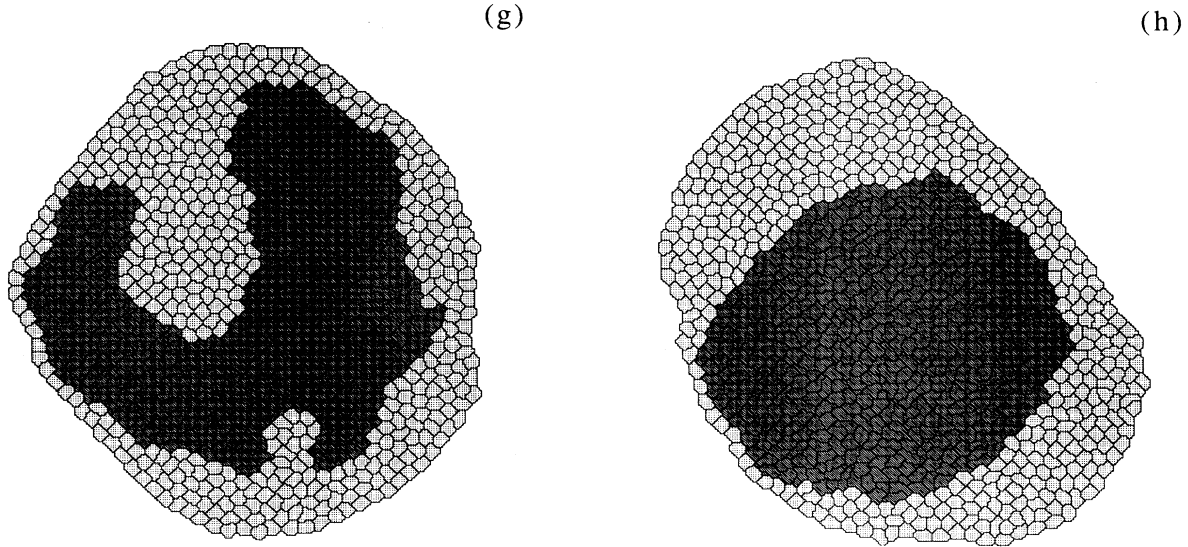


FIG. 12. (Continued).

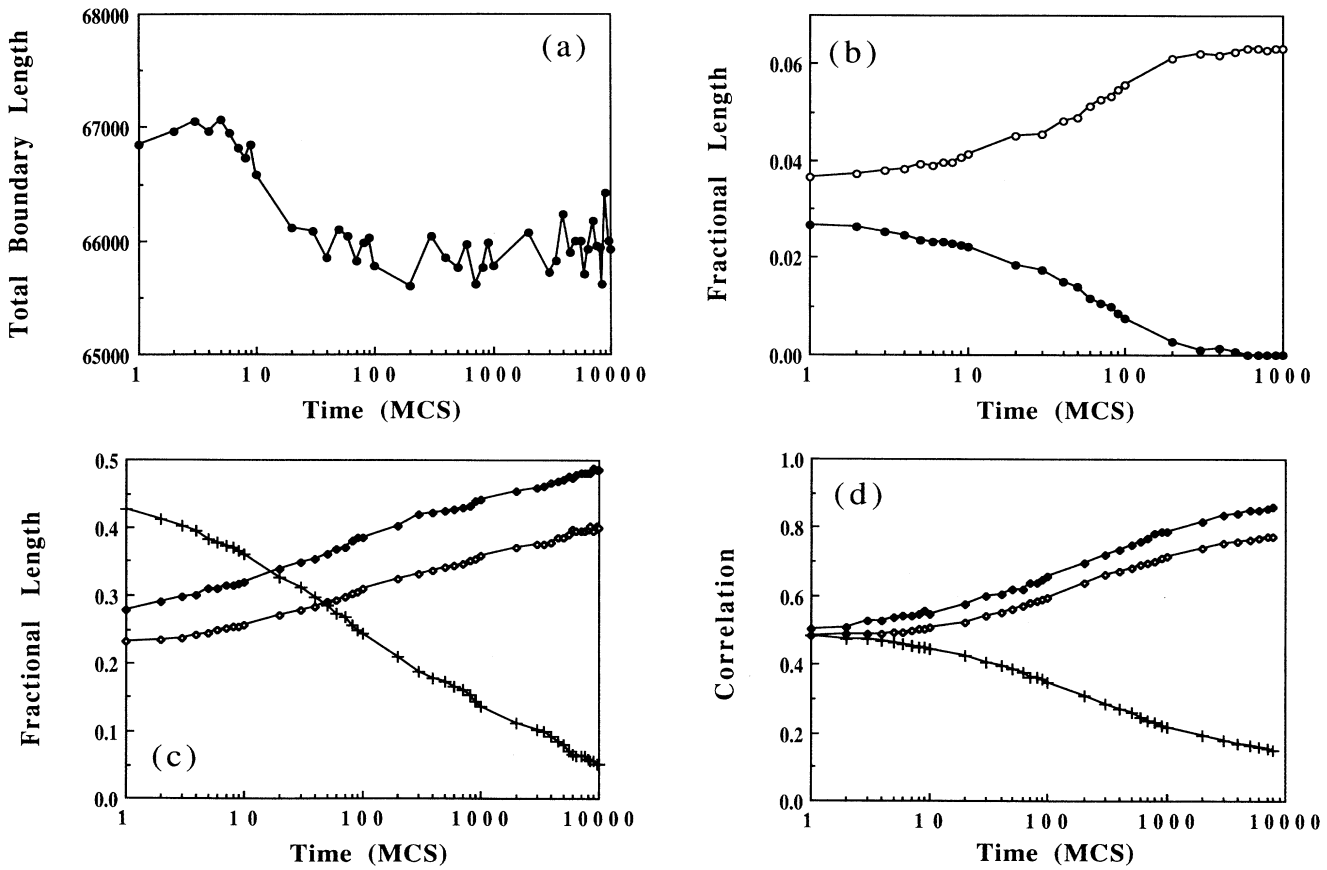


FIG. 13. Cell sorting. Simulation.  $J_{ll} = 14$ ,  $J_{dd} = 2$ ,  $J_{ld} = 11$ ,  $J_{lM} = J_{dM} = 16$  (yielding,  $\gamma_{ld} = 3$ ,  $\gamma_{lM} = 9$ ,  $\gamma_{dM} = 15$ ),  $T = 10$ , and  $\lambda = 1$ , random initial cell type assignment. Boundary lengths of the simulation shown in Fig. 12. (a) Total length. (b) Fractional contact length with the medium, light-Medium interface (circles), dark-Medium interface (bullets). (c) Fractional boundary length of cell-cell contacts, light-light homotypic (open diamonds), dark-dark homotypic (solid diamonds), light-dark heterotypic (crosses). (d) Type-type correlation, light-light homotypic (open diamonds), dark-dark homotypic (solid diamonds), light-dark heterotypic (crosses). Statistics are calculated after two MCS of  $T = 0$  annealing.

centered dark cluster and skew otherwise. However, differences in topological charge are usually screened over one cell diameter in soap froth, so the off-center position may be a metastable equilibrium [27,41]. If this phenomenon does cause a centering of the dark cluster, it occurs on a time scale too long for us to observe. In real biological systems, the cohesive cluster is often off center with respect to the aggregate as a whole [13].

We can relate an interesting biological observation to one of the preceding results. In our simulations we see a quick boundary-driven phase (600 MCS) resulting in monolayer formation, followed by a very slow ( $10^4$  MCS) bulk rearrangement. This could explain why, in *Hydra* cell aggregates, a monolayer of ectodermal cells forms over 6 h but complete bulk sorting does not occur [8]. Instead, a central cavity forms after 16 to 20 h [8,9] (see Sec. III F) and the aggregate expels unsorted cells which then die. Our simulation suggests that complete sorting in *hydra* would need on the order of  $10^2$  h, i.e., a few days, by which time the aggregate has already reconstructed its head and neural net, and almost completed its regeneration into a normal animal.

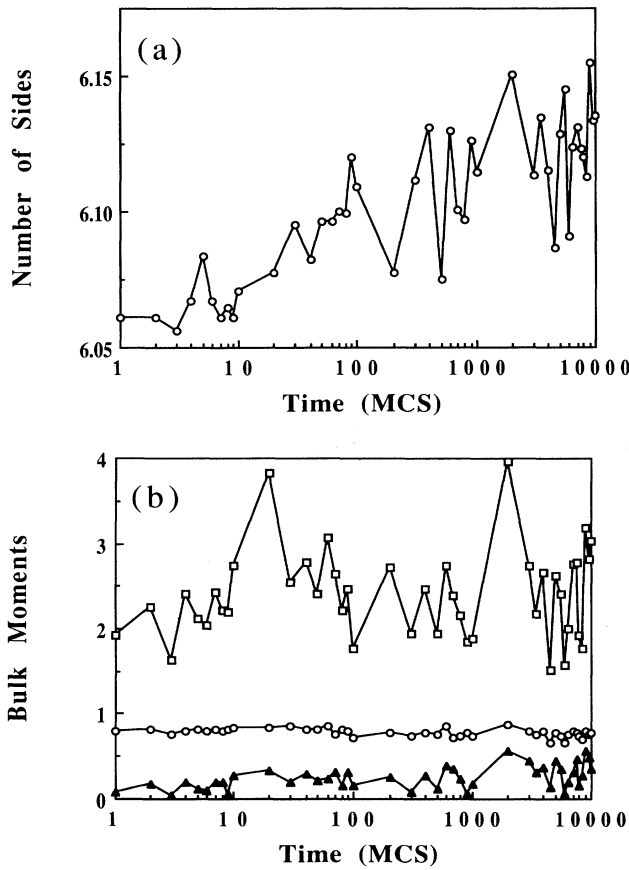


FIG. 14. Cell sorting. Simulation.  $J_{ll} = 14$ ,  $J_{dd} = 2$ ,  $J_{ld} = 11$ ,  $J_{lM} = J_{dM} = 16$  (yielding  $\gamma_{ld} = 3$ ,  $\gamma_{lM} = 9$ ,  $\gamma_{dM} = 15$ ),  $T = 10$ , and  $\lambda = 1$ , random initial cell type assignment. Topological moments of the simulation shown in Fig. 12. (a)  $\langle n \rangle$ . (b) Topological bulk moments:  $\mu_2$  (circles),  $\mu_3$  (triangles),  $\mu_4$  (squares). Statistics are calculated after two MCS of  $T = 0$  annealing.

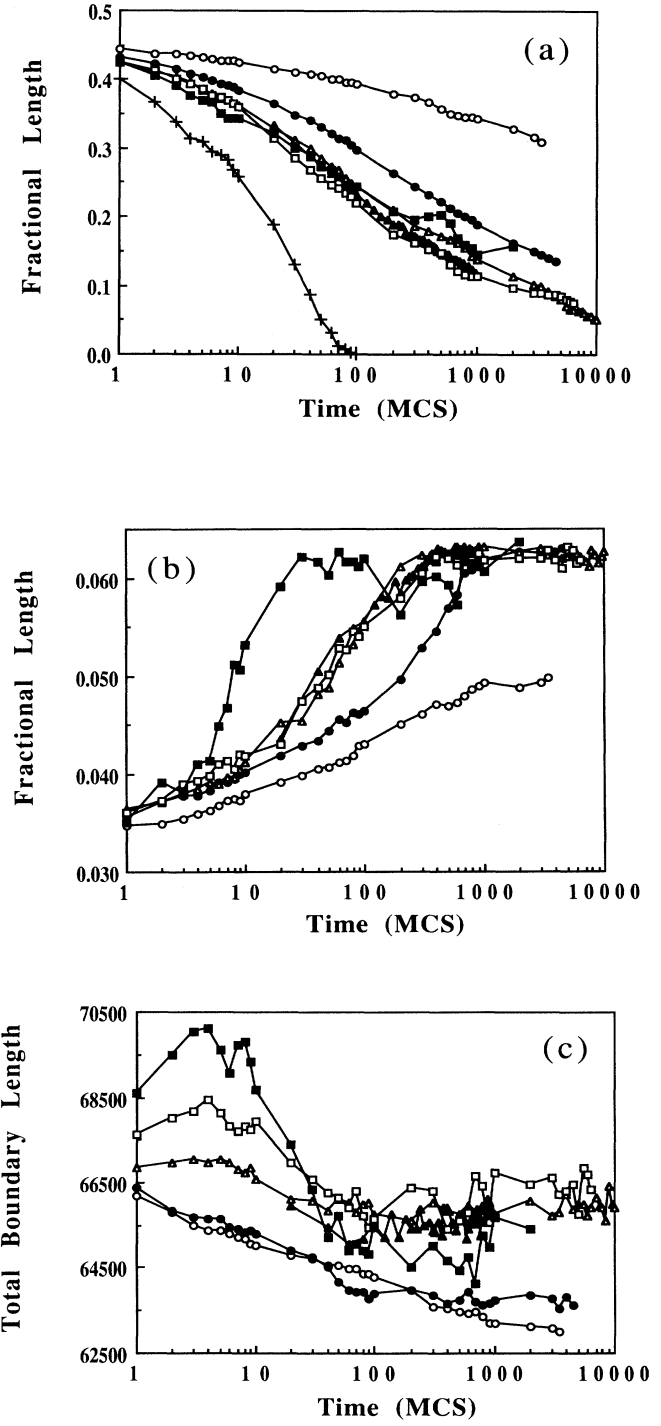


FIG. 15. Cell sorting. Simulation.  $J_{ll} = 14$ ,  $J_{dd} = 2$ ,  $J_{ld} = 11$ ,  $J_{lM} = J_{dM} = 16$  (yielding  $\gamma_{ld} = 3$ ,  $\gamma_{lM} = 9$ ,  $\gamma_{dM} = 15$ ), and  $\lambda = 1$ , identical random initial cell type assignment for each temperature. Comparison of boundary length evolution for different temperatures. (a) Light-dark heterotypic interface. (b) Light-Medium interface. (c) Total boundary length. Temperatures:  $T = 2$  (open circles),  $T = 5$  (bullets),  $T = 10$  (open triangles),  $T = 15$  (solid triangles),  $T = 20$  (open squares),  $T = 40$  (solid squares),  $T = 80$  (crosses). Statistics are calculated after two MCS of  $T = 0$  annealing.

#### 4. Temperature

As in the case of the checkerboard, a comparison of cell sorting at different temperatures for fixed  $\lambda=1$  proves instructive. If we look at the averaged bulk moments at long times (Table II) we see a consistent increase of all moments with temperature, apparently resulting from the presence of nonsimply connected cells. We show the light-dark heterotypic boundary length in Fig. 15(a), and the light-Medium boundary length in Fig. 15(b). As we did for the checkerboard, we can distinguish three regimes: a low-temperature freezing, a “normal” regime which is qualitatively independent of the temperature, and a high-temperature disordered regime.

At  $T=0$  the pattern rapidly freezes and does not sort. The  $T=2$  simulation sorts very slowly and does not form a light-cell monolayer.

For the other simulation temperatures, at short times (0–10 MCS) the boundary length is higher for higher temperatures, as we would expect from their larger thermal fluctuations. At intermediate times (10–100 MCS), the higher temperatures evolve more rapidly, resulting in some crossing of lengths [Figs. 15(a)–15(c)]. At long times (100–1000 MCS) they reach a plateau at roughly the same value. The differences in slope strongly suggest that monolayer formation depends on thermally activated processes; on the other hand, the final state is temperature independent over a fairly wide range.

The  $T=5$  simulation (although slower) and the  $T=10$ , 15, and 20 simulations form a group that sorts normally, eventually achieving the same values for all lengths; the evolution of all the total boundary lengths [Fig. 15(c)] is fairly consistent. The  $T=40$  simulation reaches a plateau beyond which thermal fluctuations prevent it from reducing its light-dark heterotypic boundary length. However, thermal fluctuations are not strong enough to prevent a light-cell monolayer from forming rapidly (50 MCS). At  $T=80$ , the light-dark interface decreases to zero because all cells are unstable and disappear; the light cells disappear more quickly because of their higher energy.

#### 5. The area constraint

Finally, we investigate the effect of the area constraint by varying  $\lambda$  at a fixed temperature of  $T=5$ . In Fig. 16(a) we plot the evolution of the total length as a function of the MCS. At low  $\lambda$  not all cells are conserved. For  $\lambda=0.1$ , all cells shrink and disappear. For  $\lambda=0.2$  all the light cells shrink and disappear but the dark cells are conserved. For  $\lambda=0.5$  a few light cells disappear, but most survive.

For values of  $\lambda$  higher than 0.5, all cells are conserved. We show the boundary length evolutions in Figs. 16(b) and 16(c). The pattern does not freeze for any of the  $\lambda$  values that we studied. Moreover, the moments appear relatively independent of  $\lambda$  except for a possible slight increase (Table III).

However,  $\lambda$  strongly affects the relative timings of bulk and surface sorting. For instance, in the bulk, higher  $\lambda$  values do not prevent cell sorting, e.g., the reduction of light-dark heterotypic boundary length, but the sorting

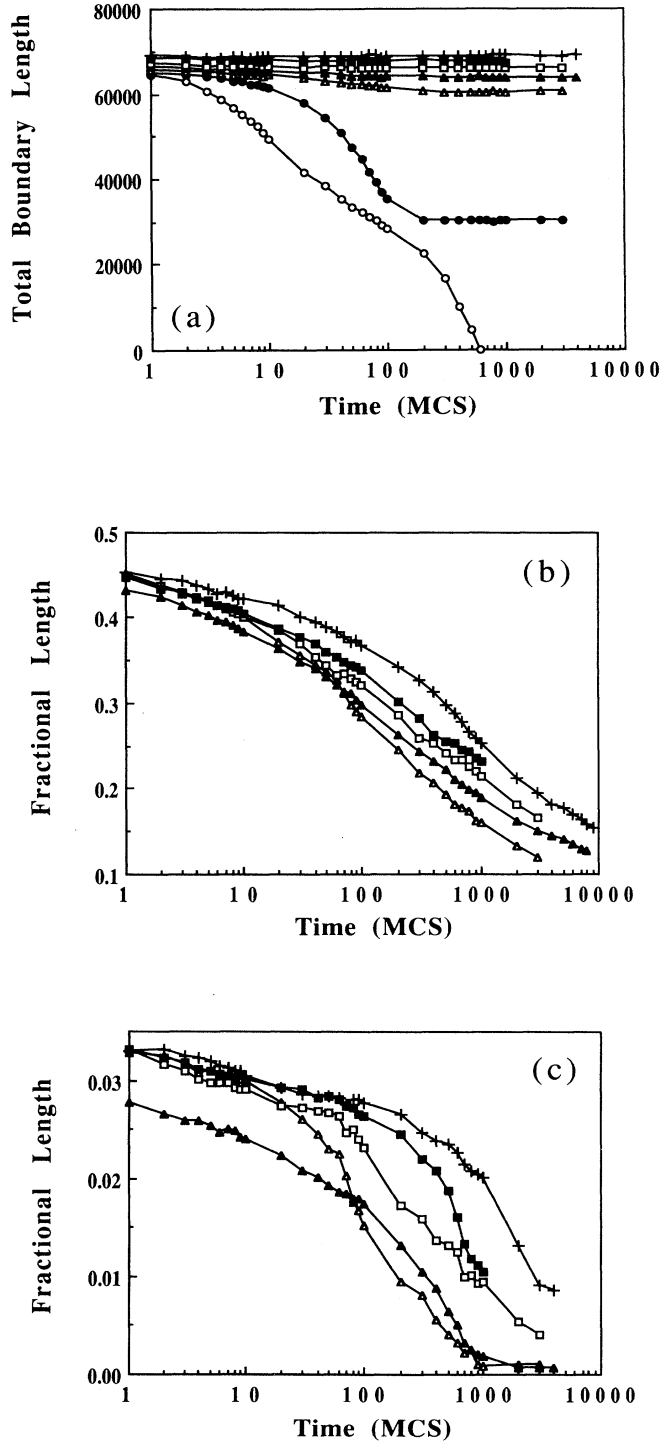


FIG. 16. Cell sorting. Simulation.  $J_{ll} = 14$ ,  $J_{dd} = 2$ ,  $J_{ld} = 11$ ,  $J_{IM} = J_{dM} = 16$  (yielding  $\gamma_{ld} = 3$ ,  $\gamma_{IM} = 9$ ,  $\gamma_{dM} = 15$ ), and  $T = 5$ , identical random initial cell type assignment for each  $\lambda$ . Comparison of boundary length evolution for different  $\lambda$ . (a) Total boundary length. (b) Light-dark heterotypic interface, (c) Dark-Medium boundary length.  $\lambda$ :  $\lambda = 0.1$  (open circles),  $\lambda = 0.2$  (bullets),  $\lambda = 0.5$  (open triangles),  $\lambda = 1$  (solid triangles),  $\lambda = 2$  (open squares),  $\lambda = 5$  (solid squares),  $\lambda = 10$  (crosses). Statistics are calculated after two MCS of  $T = 0$  annealing.

TABLE III. Averaged bulk moments of the cell sorting as a function of  $\lambda$ . Statistics are calculated after two MCS of  $T=0$  annealing. Errors are one standard deviation. Note that cells are unstable for  $\lambda=0.1$  and 0.2, so the average is over a changing light-dark population.

$\lambda$	$\langle n \rangle$	$\mu_2$	$\mu_3$	$\mu_4$
0.1	$6.02 \pm 0.01$	$0.79 \pm 0.12$	$0.01 \pm 0.10$	$1.89 \pm 0.72$
0.2	$6.02 \pm 0.02$	$0.72 \pm 0.04$	$0.06 \pm 0.07$	$1.55 \pm 0.24$
0.5	$6.02 \pm 0.01$	$0.57 \pm 0.04$	$0.00 \pm 0.05$	$1.08 \pm 0.14$
1.0	$6.02 \pm 0.01$	$0.50 \pm 0.04$	$0.01 \pm 0.03$	$0.88 \pm 0.11$
2.0	$6.03 \pm 0.01$	$0.55 \pm 0.03$	$0.01 \pm 0.02$	$0.99 \pm 0.12$
5.0	$6.04 \pm 0.01$	$0.57 \pm 0.04$	$0.00 \pm 0.05$	$1.10 \pm 0.18$
10.0	$6.06 \pm 0.02$	$0.57 \pm 0.03$	$0.04 \pm 0.05$	$1.11 \pm 0.12$

for  $\lambda=10$  is ten times slower than for  $\lambda=0.5$  [Fig. 16(b)]. The change is even more dramatic for the formation of the surface light-cell monolayer, which slows by nearly a factor of 50 [Fig. 16(c)]. Indeed, it is not clear that a true monolayer will ever form in the limit of large  $\lambda$ . Certainly, the monolayer will form after the bulk has finished sorting, a striking qualitative change in the pattern evolution. This effect of cell rigidity on time scales should also be observable in biological tissues [42].

### C. Engulfment

A different initial condition involves contact between two compact masses of different cell types. In such experiments, aggregates of two different types are brought into contact in hanging droplets so that there is no interference from a substrate. Such experiments usually yield the same final configuration as cell sorting from an initial mixed aggregate [6,14]. This result supports Steinberg's idea that global energy minimization determines the final configuration. In Fig. 17, we show an experimental study of Armstrong of pigmented retinal cells engulfing heart cells in chicken embryo cell aggregates. Similarly, recombination between intact portions of *hydra* endoderm and ectoderm yields quick engulfment in a process similar to aggregate regeneration [43].

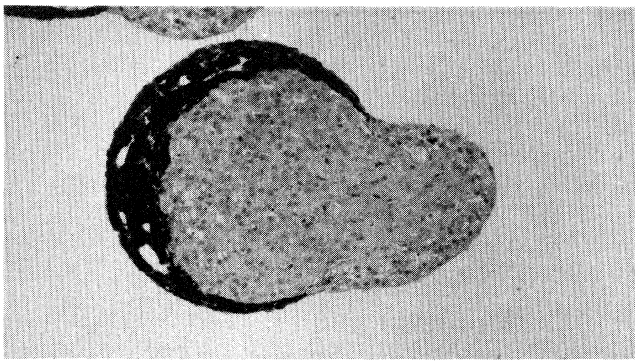


FIG. 17. Engulfment. Observation by Armstrong of cell engulfment of heat cells (light) by pigmented retinal cells (dark) from tenth-day chicken embryo in three-dimensional suspended aggregates. Reprinted with permission from P. Armstrong, Crit. Rev. Biochem. and Mol. Biol. **24**, 119 (1989). Copyright CRC Press, Inc., Boca Raton, FL. Figure shows a two-dimensional section of a three-dimensional culture after 48 h.

In Fig. 18 we show a simulation of this situation, where we begin with our equilibrated pattern with the top half assigned to light cells and the bottom half to dark cells [Fig. 18(a)]. The energies are identical to the cell-sorting case:  $J_{ll}=14$ ,  $J_{dd}=2$ ,  $J_{ld}=11$ ,  $J_{lM}=J_{dM}=16$  (yielding  $\gamma_{ld}=3$ ,  $\gamma_{lM}=9$ ,  $\gamma_{dM}=15$ ),  $T=10$ , and  $\lambda=1$ . Engulfment does occur but is very slow [Figs. 18(b) and 18(c)], with the light-cell monolayer still not complete after 10 000 MCS [Fig. 18(d)].

However, if we look at the boundary lengths as a function of time [Figs. 19(a) and 19(b)], the migration shows no evidence of logarithmic slowing down; that is, it is spontaneous. Only the few spins at the triple light-dark-Medium vertex experience directly the surface tension caused by the light-Medium, dark-Medium energy difference. These spins in turn drag the whole bulk of the light cells behind them. As the triple point moves forward, it must drag an ever-increasing mass of light monolayer, gradually slowing the evolution. Note that dark cells sometimes break through the light-cell monolayer, which does not occur in normal cell sorting [Figs. 18(a) and 18(d)]. The breakthrough is due to thermal fluctuations, without which the front spins would pin and evolution would cease.

The total boundary length equilibrates after about 1000 MCS, with the moments equilibrating after about 100 MCS ( $\langle n \rangle=6.14 \pm 0.03$ ,  $\mu_2=0.76 \pm 0.06$ ,  $\mu_3=0.39 \pm 0.15$ ,  $\mu_4=2.81 \pm 0.74$ ). The correlation functions, of course, do not equilibrate within the duration of the run. A simple extrapolation, e.g., a linear fit ( $R^2=0.987$ ), suggests that it would take about 11 000 MCS for complete engulfment.

The same slow engulfment occurs in the Voronoi model for cell sorting, in which engulfment is six to ten times slower than normal cell sorting [33]. The Voronoi model engulfs faster than the Potts model, however, because a single cell drags the monolayer, rather than a single spin exactly at the triple contact. We expect the evolution to be much faster in three dimensions, and also in biological aggregates, where a one-dimensional line of cells drags a two-dimensional monolayer and in which cell motions are less constrained.

### D. Position reversal

Occasionally in biological systems there is an apparent reversal of the light-dark order described above, with a layer of cohesive dark cells surrounding a layer of less

cohesive light cells [6]. In spite of the adhesivity differences, such a reversed pattern is the true energy minimum, since it forms when the dark cells have a lower surface tension with the medium [23].

There are many other possible initial conditions of biological relevance. For example, if no dark cells are initially in contact with the medium, we expect normal cell sorting to follow, since the dark cells have no opportunity to sort outwards [44]. However, we have not investigated these initial conditions. What we want to do here is only to show that we successfully reproduce biologically observed behaviors for various combinations of surface tensions, whatever the actual surface energies (which act on each cell's shape and movement, but not on the global configuration).

In our simulation we use a (very) large energy between the medium and the light cells. Our energies are  $J_{ll}=14$ ,  $J_{IM}=30$ ,  $J_{dd}=2$ ,  $J_{dM}=16$ ,  $J_{ld}=11$  (yielding  $\gamma_{ld}=3$ ,  $\gamma_{IM}=23$ ,  $\gamma_{dM}=15$ ),  $T=10$ , and  $\lambda=1$ . We show an early

and a late state of the simulation evolution in Fig. 20.

All of the moments are equilibrated by ten MCS. The large  $\gamma_{IM}$  causes some unusual cell shapes in Fig. 20(b). The dark cells initially in contact with the medium stretch rapidly to create a dark monolayer (complete by 40 MCS). The monolayer cells remain stretched until the outward diffusion of additional dark cells allows them to form a monolayer without stretching. In spite of this cell stretching, the moments for the bulk and entire pattern are the same within error:  $\langle n \rangle = 6.08 \pm 0.03$ ,  $\mu_2 = 0.71 \pm 0.06$ ,  $\mu_3 = 0.24 \pm 0.14$ ,  $\mu_4 = 2.40 \pm 0.65$ .

After this initial transient, the correlation functions and boundary lengths [Figs. 21(a) and 21(b)] show two other regimes. Until about 200 MCS, sorting accelerates. The surface cells still show stretching at 500 MCS [Fig. 20(c)], and achieving completely normal surface cell shapes requires approximately 1000 MCS. Then, segregation and coalescence of light cells gradually slow down, since puncturing continuous ribbons of cohesive dark

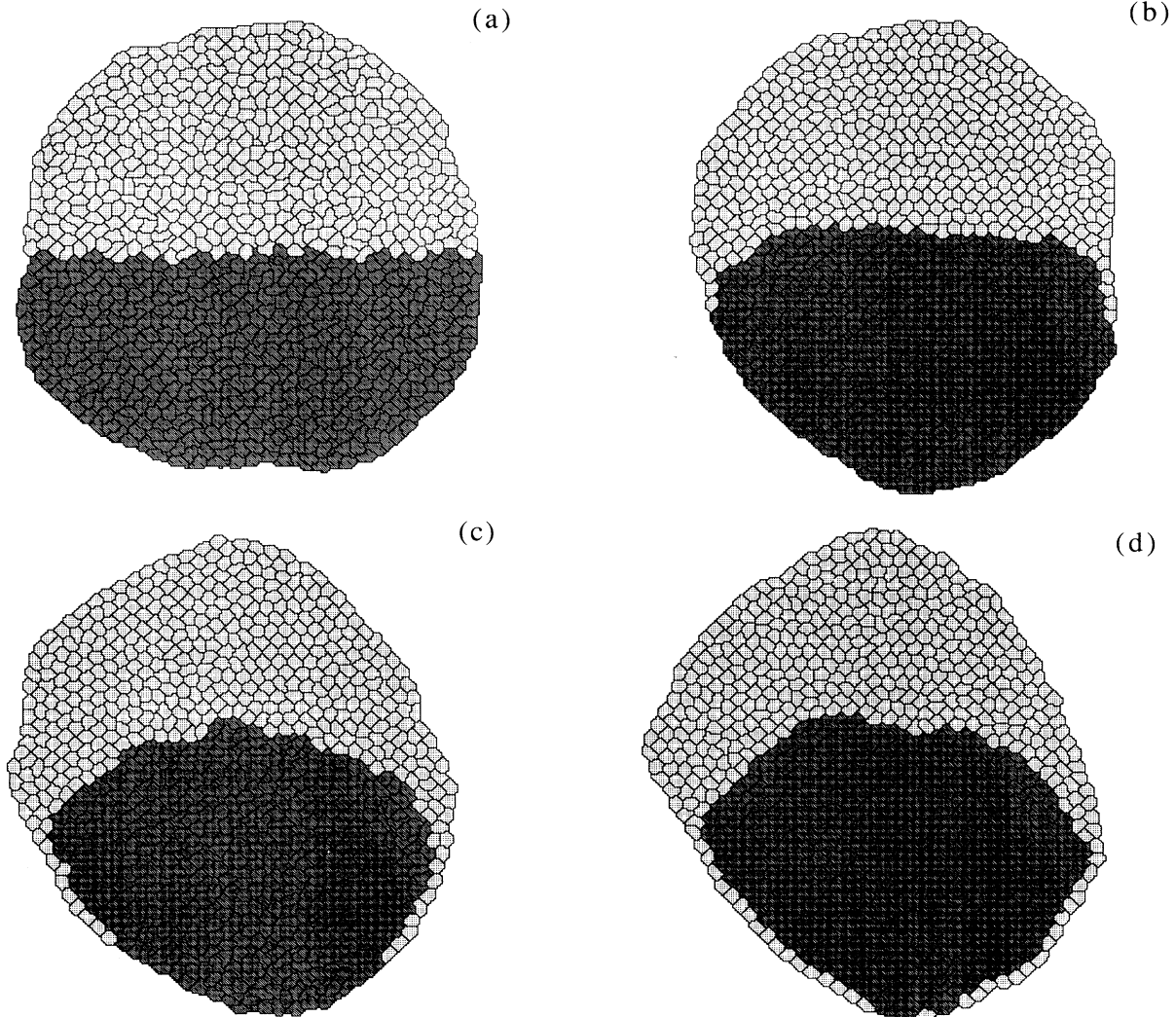


FIG. 18. Engulfment. Simulation.  $J_{ll}=14$ ,  $J_{dd}=2$ ,  $J_{ld}=11$ ,  $J_{IM}=J_{dM}=16$  (yielding  $\gamma_{ld}=3$ ,  $\gamma_{IM}=9$ ,  $\gamma_{dM}=15$ ), and  $\lambda=1$ , initial cell type assignment upper half light, lower half dark. (a) Initial condition, 0 MCS. (b) 1000 MCS. (c) 5000 MCS. (d) 10 000 MCS.  $\langle n \rangle = 6.14 \pm 0.03$ ,  $\mu_2 = 0.76 \pm 0.06$ ,  $\mu_3 = 0.39 \pm 0.15$ ,  $\mu_4 = 2.81 \pm 0.74$ . Patterns are displayed after two MCS of  $T=0$  annealing.

cells is an activated processes with a high-energy barrier which comes to dominate the sorting. Multiple light-cell regions still persist at 5000 MCS [Fig. 20(d)].

### E. Partial cell sorting

#### 1. Description of the phenomenon

Sometimes the sorting of cell types in an initially mixed aggregate remains incomplete. Clusters of each cell type form and grow, but never reach the final state of two connected concentric regions. Instead, the main clusters trap other large heterotypic clusters. The final state resembles that shown in Figs. 10(b) and 11(b). Trapping occurs biologically, e.g., in chicken embryo cells. It is sensitive to the geometry, initial conditions, and respective cell proportions [6,13,32,45].

In these observations, homotypic clusters are probably

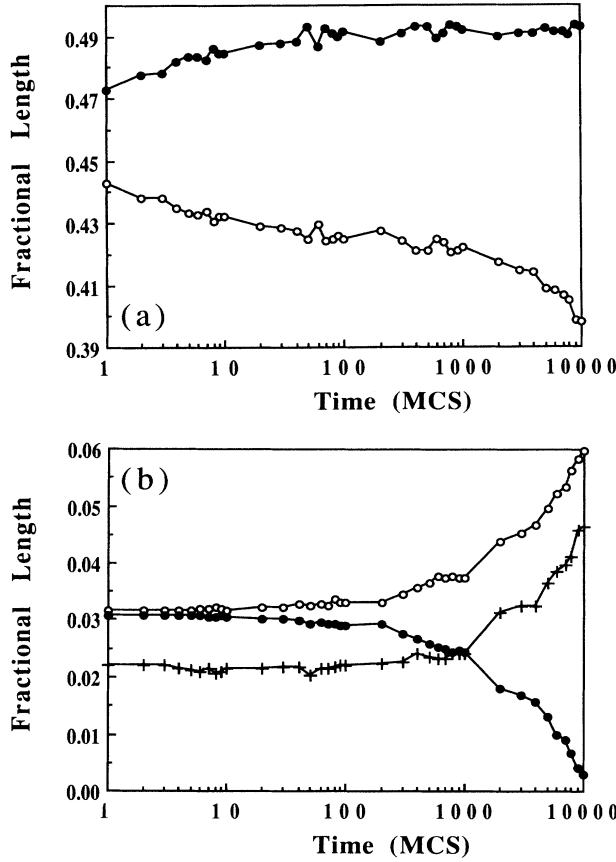


FIG. 19. Engulfment. Simulation.  $J_{ll} = 14$ ,  $J_{dd} = 2$ ,  $J_{ld} = 11$ ,  $J_{IM} = J_{dM} = 16$  (yielding  $\gamma_{ld} = 3$ ,  $\gamma_{IM} = 9$ ,  $\gamma_{dM} = 15$ ), and  $\lambda = 1$ , initial cell type assignment upper half light, lower half dark. (a) Fractional homotypic boundary length, light-light homotypic (open diamonds), dark-dark homotypic (solid diamonds). (b) Fractional heterotypic contact length, light-Medium interface (circles), dark-Medium interface (bullets), light-dark heterotypic (crosses). Statistics are calculated after two MCS of  $T=0$  annealing.

unable to travel long distances [24]. In an aggregate with either a very-two-dimensional geometry or a very heterogeneous initial distribution of light and dark cells, homotypic clusters are distant and have a low probability to encounter and fuse. Similarly, if the overall number of light and dark cells is very unequal, clusters of the minority type have a smaller probability to encounter each other, and complete cell sorting occurs only above a percolation threshold for the minority percentage. However, since dark cells sort inwards and light cells sort towards the boundary to form a monolayer, their respective percolation thresholds need not be the same.

What we want to investigate here is the specific effect of surface tensions on sorting. Can the value of  $\gamma_{ld}$  tune the sorting from total to partial?  $\gamma_{ld}$  can determine what configuration has the minimum energy. When  $\gamma_{ld}$  is greater than  $\gamma_{dM} - \gamma_{IM}$ , the three interfaces, light-dark, light-Medium and dark-Medium, are stable and meet at angles obeying the Young condition. Thus at equilibrium the light cells do not completely surround the dark-cell mass.

In addition to this static effect, does  $\gamma_{ld}$  affect the dynamics of sorting? We suggest that in complete cell sorting, the movement of light-cell clusters is energetically neutral so that they can escape by diffusion, but that such escape is more difficult for a high  $\gamma_{ld}$ , resulting in partial cell sorting. We simulate this situation by reversing the normal cell-sorting energy relation  $J_{ll} > J_{ld}$ , keeping all other surface energies the same while exchanging  $J_{ll}$  and  $J_{ld}$ . We therefore simulate with  $J_{ll} = 11$ ,  $J_{dd} = 2$ ,  $J_{ld} = 14$ ,  $J_{IM} = J_{dM} = 16$  (yielding  $\gamma_{ld} = 7.5$ ,  $\gamma_{IM} = 10.5$ ,  $\gamma_{dM} = 15$ ),  $T = 5$ , and  $\lambda = 1$ .

#### 2. Early sorting

We show the evolution of such a simulation in Fig. 22. We begin with our standard equilibrated random state. The initial rapid clustering is nearly identical to normal cell sorting [compare at ten MCS Figs. 12(b) and 22(a)], though the higher light-dark interface energy results in smoother, rounder boundaries between the clusters. At 100 MCS the clusters of the two patterns are still similar in wavelength [Figs. 12(c) and 22(b)]. If we evaluate the bulk moments for times after 100 MCS, we obtain  $\langle n \rangle = 6.03 \pm 0.01$ ,  $\mu_2 = 0.57 \pm 0.03$ ,  $\mu_3 = 0.02 \pm 0.04$ , and  $\mu_4 = 1.1 \pm 0.1$ .

However, the normal cell sorting has nearly completed its external light-cell monolayer while the partial cell sorting has not. The failure to form a monolayer is due to the Young condition being satisfied on the edge of the aggregate; i.e., even though the light-Medium interface has a relatively lower energy cost, the dark-Medium interface is still stable and can only be destroyed by the diffusion of light cells to the aggregate edge.

#### 3. Cluster sorting

The differences between partial and total sorting are much more clear at 1000 MCS [Figs. 12(d) and 22(c)]. The clusters in the partial cell-sorting case still contain

many small heterotypic inclusions. Even after 2000 MCS [Fig. 22(d)] there is no sign of the disappearance of small dark-cell clusters and no monolayer forms. The high  $J_{ld}$  energy barrier now blocks diffusion of small clusters, drastically slowing their migration. This slowing is not an artifact of the Potts model, and it is probably true, for small clusters of actual cells, that any movement is more costly if  $J_{ld}$  is higher.

The main contribution to the decrease in heterotypic contact length now comes from spontaneous cluster rounding, rather than the coalescence of diffusing clusters. This rounding is slow but steady, hence the extremely smooth logarithmic evolution [Fig. 23(a)]. By rounding, a cluster can come into contact with other clusters and coalesce, but with a much smaller probability than for a mobile diffusing cluster.

If we look at the cell-cell boundary lengths [Fig. 23(a)] we find that their evolution is logarithmic at all times. If

we plot them together with the total sorting case [Fig. 24(a)], the discrepancy is clear; the logarithmic fit is slightly less good ( $R^2=0.94$  rather than 0.999), probably because of the larger counting error. There does not appear to be any period in the evolution which is spontaneous as opposed to activated; the same applies to the aggregate-Medium boundary lengths [Figs. 23(b) and 24(b)]. Thus it appears that partial cell sorting in the Potts model is even more sensitive to temperature than normal cell sorting.

## F. Dispersal

### 1. Light-light cell dispersal

Even a small change in the surface tension caused, for example, by a slight quantitative or qualitative change in

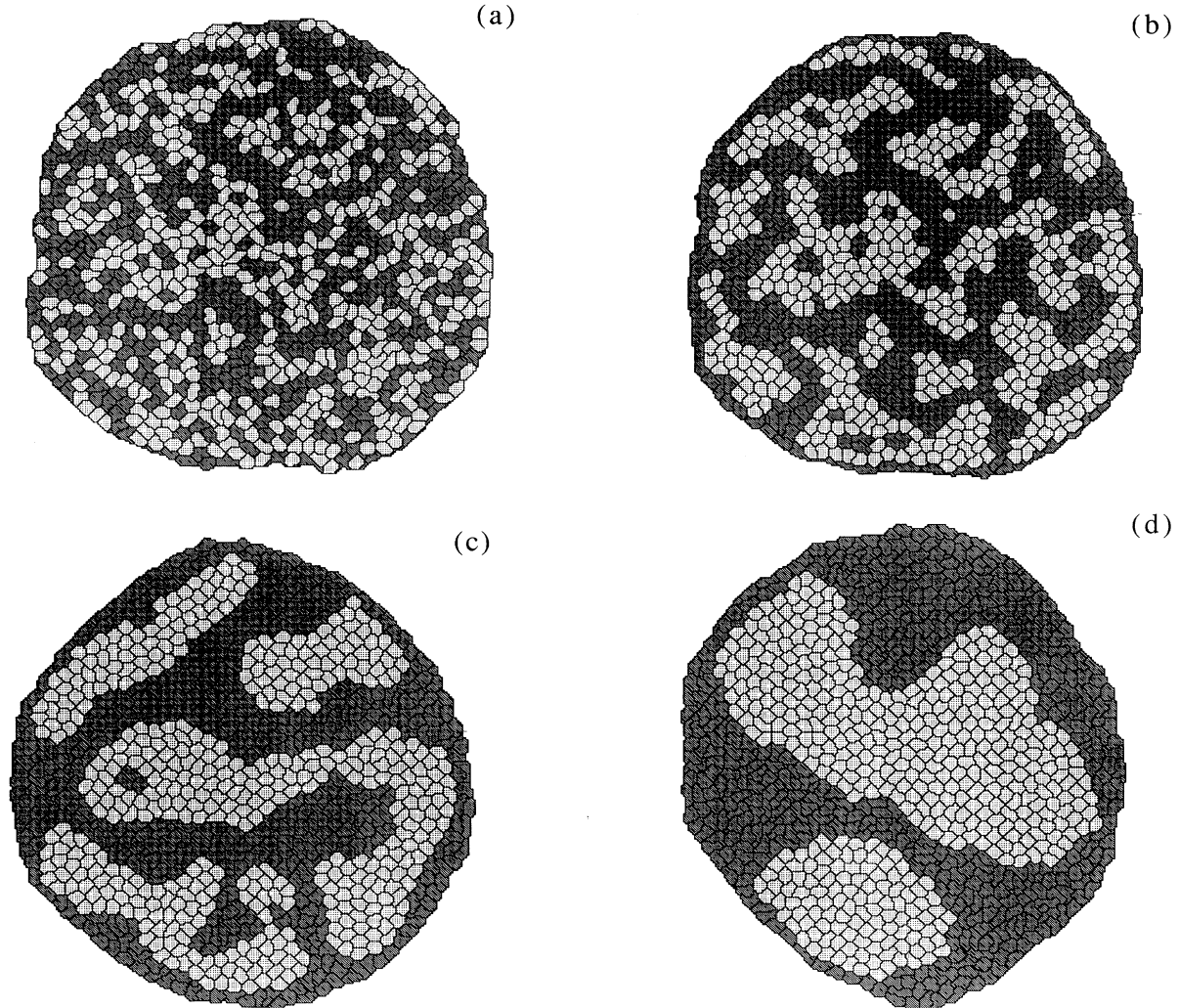


FIG. 20. Position reversal. Simulation.  $J_{ll}=14$ ,  $J_{lM}=30$ ,  $J_{dd}=2$ ,  $J_{dM}=16$ ,  $J_{ld}=11$  (yielding  $\gamma_{ld}=3$ ,  $\gamma_{lM}=23$ ,  $\gamma_{dM}=15$ ),  $T=10$ , and  $\lambda=1$ , random initial cell type assignment. (a) Initial condition, 0 MCS. (b) 50 MCS. (c) 5000 MCS. (d) 5000 MCS.  $\langle n \rangle=6.08\pm 0.03$ ,  $\mu_2=0.71\pm 0.06$ ,  $\mu_3=0.24\pm 0.14$ ,  $\mu_4=2.40\pm 0.65$ . Patterns are displayed after two MCS of  $T=0$  annealing.

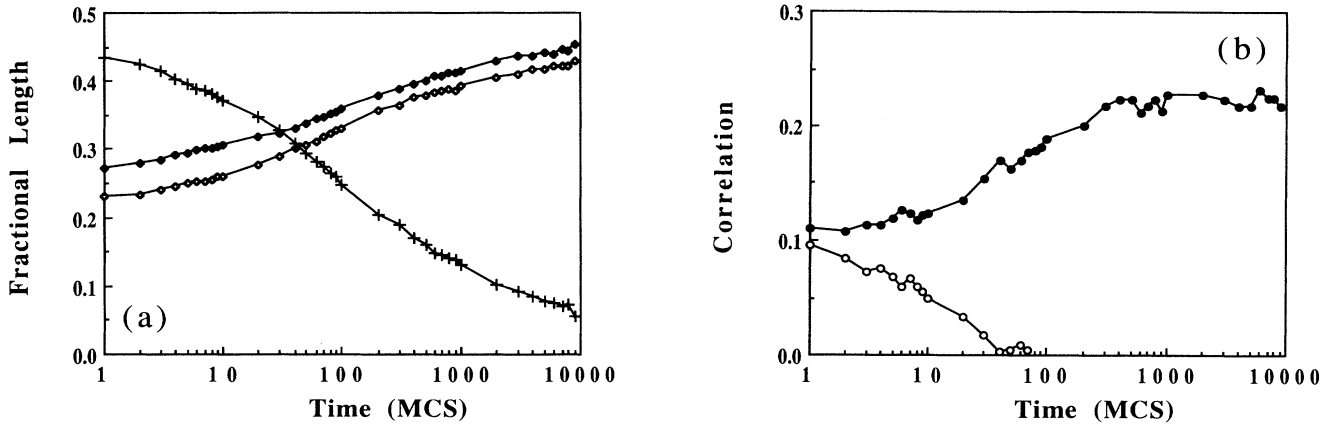


FIG. 21. Position reversal. Simulation.  $J_{ll} = 14$ ,  $J_{lM} = 30$ ,  $J_{dd} = 2$ ,  $J_{dM} = 16$ ,  $J_{ld} = 11$  (yielding  $\gamma_{ld} = 3$ ,  $\gamma_{lM} = 23$ ,  $\gamma_{dM} = 15$ ),  $T = 10$ , and  $\lambda = 1$ , random initial cell type assignment. (a) Fractional boundary length of cell-cell contacts, light-light homotypic (open diamonds), dark-dark homotypic (solid diamonds), light-dark heterotypic (crosses). (b) Type-type correlation, light-Medium (open circles), dark-Medium (bullets). Statistics are calculated after two MCS of  $T = 0$  annealing.

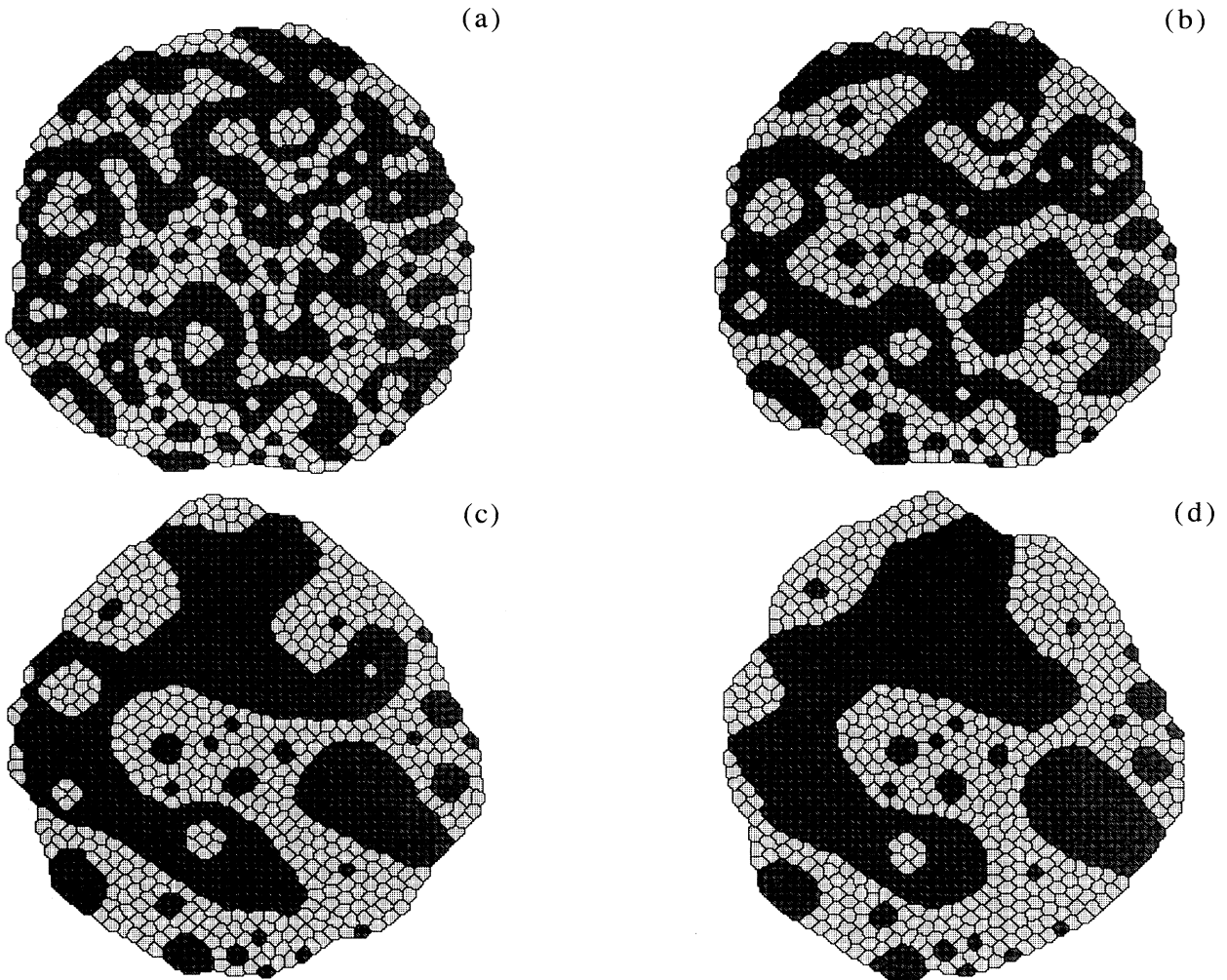


FIG. 22. Partial cell sorting. Simulation.  $J_{ll} = 11$ ,  $J_{dd} = 2$ ,  $J_{ld} = 14$ ,  $J_{lM} = J_{dM} = 16$  (yielding  $\gamma_{ld} = 7.5$ ,  $\gamma_{lM} = 10.5$ ,  $\gamma_{dM} = 15$ ),  $T = 5$ ,  $\lambda = 1$ , random initial cell type assignment. (a) 10 MCS, (b) 100 MCS, (c) 1000 MCS, (d) 2000 MCS. Patterns are displayed after two MCS of  $T = 0$  annealing.

the expression of specialized surface adhesion molecules can result in a drastic change in the properties of an aggregate [16]. If we increase  $J_{ll}$  or decrease  $J_{IM}$  so that  $J_{ll} > J_{IM}$ , resulting in a negative light-Medium surface tension, then a spectacular change occurs. Any light cells which come into contact with the medium separate from the aggregate as isolated cells surrounded by medium. Meanwhile, the dark cells continue to coalesce (or similarly *mutatis mutandis* for  $J_{dd}$  and  $J_{dM}$ ). We show such a simulation, with  $J_{ll}=14$ ,  $J_{dd}=4$ ,  $J_{ld}=11$ ,  $J_{IM}=2$ ,  $J_{dM}=16$  (yielding  $\gamma_{ld}=2$ ,  $\gamma_{IM}=-5$ ,  $\gamma_{dM}=14$ ),  $T=5$ , and  $\lambda=1$  in Fig. 25. Such sloughing also occurs when cells die.

## 2. Light-dark cell dispersal

A more interesting case occurs if we make our partial cell sorting more extreme by increasing  $J_{ld}$ . In this case, the surface tensions all remain positive, but the Young condition cannot be satisfied between light and dark cells.

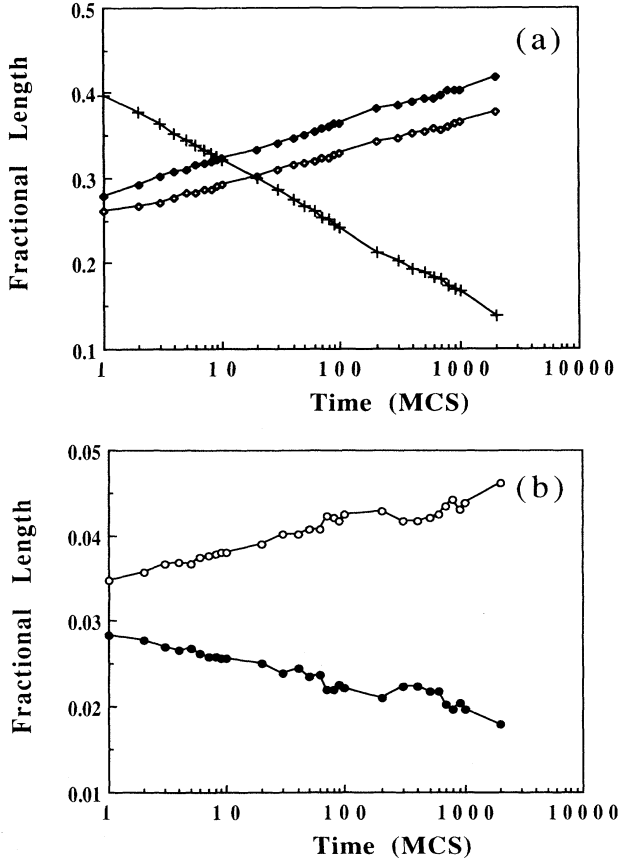


FIG. 23. Partial cell sorting. Simulation.  $J_{ll}=11$ ,  $J_{dd}=2$ ,  $J_{ld}=14$ ,  $J_{IM}=J_{dM}=16$  (yielding  $\gamma_{ld}=7.5$ ,  $\gamma_{IM}=10.5$ ,  $\gamma_{dM}=15$ ),  $T=5$ , and  $\lambda=1$ , random initial cell type assignment. (a) Fractional boundary length of cell-cell contacts, light-light homotypic (open diamonds), dark-dark homotypic (solid diamond), light-dark heterotypic (crosses). (b) Fractional contact length with the medium, light-Medium interface (circles), dark-Medium interface (bullets), light-Medium interface normal cell sorting (open squares), dark-Medium interface partial cell sorting (solid squares), dark-Medium interface normal cell sorting (solid squares). Statistics are calculated after two MCS of  $T=10$  annealing.

Thus the light and dark clusters separate. We show such a simulation with  $J_{ll}=14$ ,  $J_{dd}=2$ ,  $J_{ld}=35$ ,  $J_{IM}=J_{dM}=16$  (yielding  $\gamma_{ld}=27$ ,  $\gamma_{IM}=9$ ,  $\gamma_{dM}=15$ ),  $T=5$ , and  $\lambda=1$  in Fig. 26. Note that even a very slight decrease of  $J_{ld}$  results in partial cell sorting (Sec. III E) instead of dispersal. We show an example with  $J_{ll}=14$ ,  $J_{dd}=2$ ,  $J_{ld}=29$ ,  $J_{IM}=J_{dM}=16$  (yielding  $\gamma_{ld}=21$ ,  $\gamma_{IM}=9$ ,  $\gamma_{dM}=15$ ),  $T=5$  and  $\lambda=1$  in Fig. 27.

## 3. Cavities

More complicated examples of vacancy nucleation occur in gastrulation, or when a compact *hydra* cell aggregate separates its surface bilayer from the mass of cells in its center, and then expels the central cells [8,9,45]. However, while we can simulate the nucleation of a fluid-filled hole with the extended Potts model by changing the target areas of the cell types to be unequal [Fig.

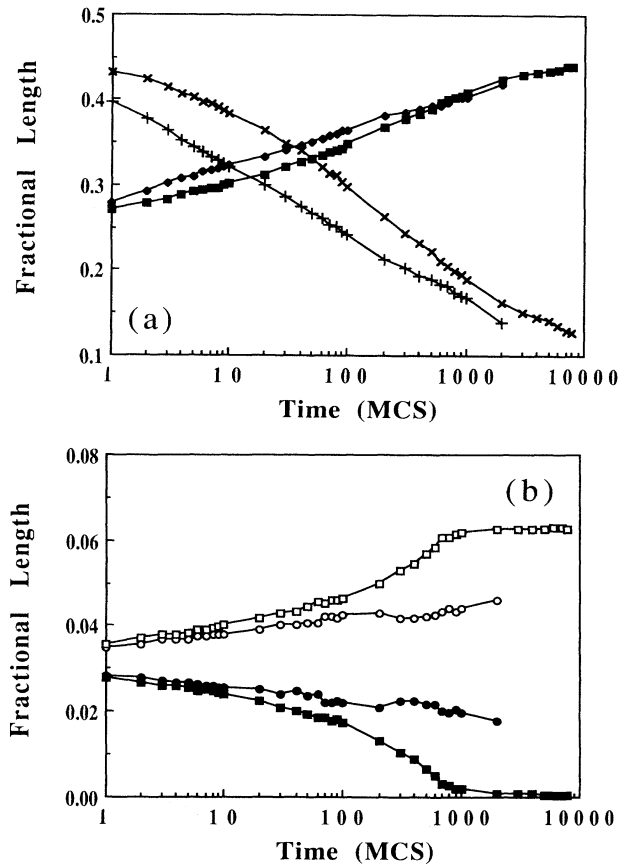


FIG. 24. Partial cell sorting. Simulation. Comparison between statistics shown in Figs. 13 and 23(a). (a) Fractional boundary length of cell-cell contacts, dark-dark homotypic partial cell sorting (solid diamonds), dark-dark homotypic normal cell sorting (solid squares), light-dark heterotypic partial cell sorting (crosses), light-dark heterotypic normal cell sorting (X's). (b) Fractional contact length with the medium, light-Medium interface partial cell sorting (circles), light-Medium interface normal cell sorting (open squares), dark-Medium interface partial cell sorting (bullets), dark-Medium interface normal cell sorting (solid squares). Statistics are calculated after two MCS of  $T=0$  annealing.

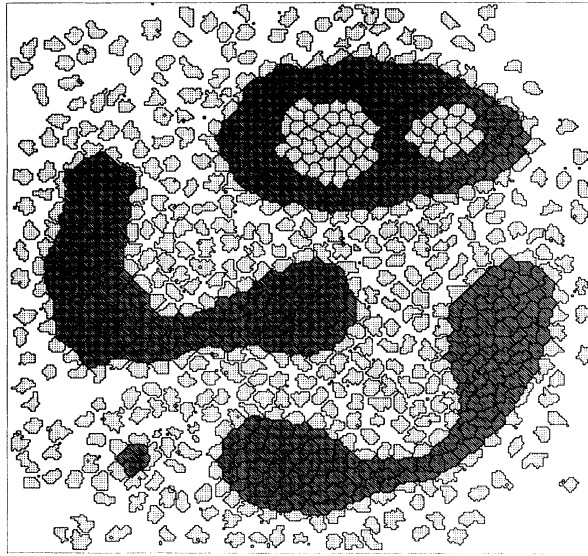


FIG. 25. Cell dispersal. Simulation.  $J_{ll}=14$ ,  $J_{dd}=4$ ,  $J_{ld}=11$ ,  $J_{IM}=2$ ,  $J_{dM}=16$  (yielding  $\gamma_{ld}=2$ ,  $\gamma_{IM}=-5$ ,  $\gamma_{dM}=14$ ),  $T=5$ , and  $\lambda=1$ , random initial cell type assignment. 480 MCS. Dark cells remain compact and round, light cells in contact with the medium disperse. Displayed pattern is unannealed.

28 shows such a case with  $J_{ll}=14$ ,  $J_{dd}=2$ ,  $J_{ld}=11$ ,  $J_{IM}=J_{dM}=16$  (yielding  $\gamma_{ld}=3$ ,  $\gamma_{IM}=9$ ,  $\gamma_{dM}=15$ ),  $T=5$ , and  $\lambda=1$ ], we are not able to stabilize it against later contraction and disappearance. In real *hydra* aggregates, it appears that the stabilization of the nucleated hole depends on qualitative changes in the contact surfaces between individual cells [46], particularly the ap-

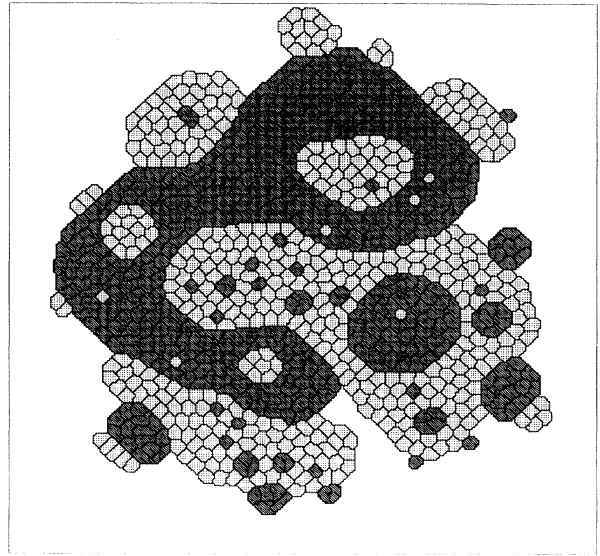


FIG. 27. Cell dispersal. Simulation.  $J_{ll}=14$ ,  $J_{dd}=2$ ,  $J_{ld}=29$ ,  $J_{IM}=J_{dM}=16$  (yielding  $\gamma_{ld}=21$ ,  $\gamma_{IM}=9$ ,  $\gamma_{dM}=15$ ),  $T=5$ , and  $\lambda=1$ , random initial cell type assignment. 2000 MCS. Both light and dark cells remain compact and round, clusters do not separate. The result is an extreme case of partial cell sorting. Pattern is displayed after two MCS of  $T=0$  annealing.

pearance of gap junctions and other junctions within the endodermal and ectodermal monolayers [47] and the synthesis of a mesoglea between the layers [45,46]. We hope to investigate this possibility further in later papers.

#### IV. CONCLUSION

Using a single model which includes only differential surface energies and an area constraint, with isotropic cells and without including detailed membrane or cytoskeletal properties, we have reproduced various observed biological phenomena of cell sorting between two

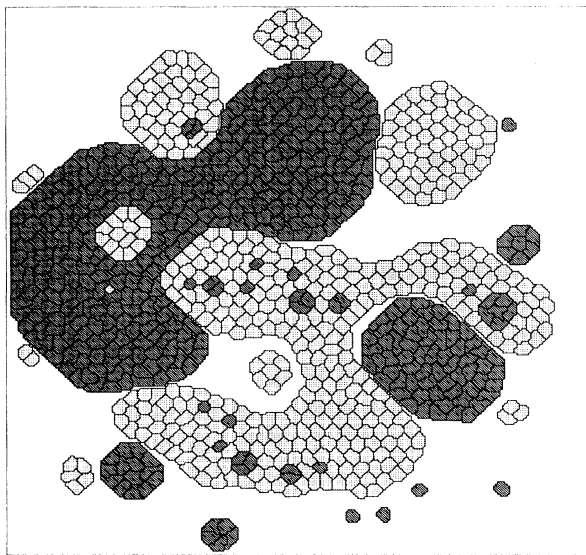


FIG. 26. Cell dispersal. Simulation.  $J_{ll}=14$ ,  $J_{dd}=2$ ,  $J_{ld}=35$ ,  $J_{IM}=J_{dM}=16$  (yielding  $\gamma_{ld}=27$ ,  $\gamma_{IM}=9$ ,  $\gamma_{dM}=15$ ),  $T=5$ , and  $\lambda=1$ , random initial cell type assignment. 2000 MCS. Both light and dark cells remain compact and round, but the clusters separate. A few isolated dark cells also occur. Pattern is displayed after two MCS of  $T=0$  annealing.

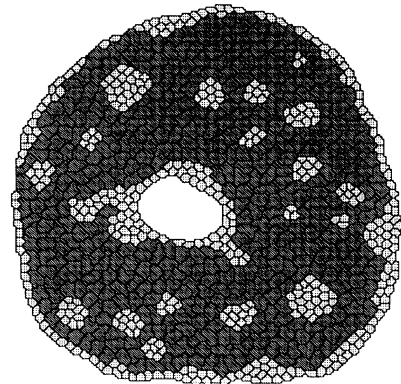


FIG. 28. Vacancy nucleation. Simulation.  $J_{ll}=14$ ,  $J_{dd}=2$ ,  $J_{ld}=11$ ,  $J_{IM}=J_{dM}=16$  (yielding  $\gamma_{ld}=3$ ,  $\gamma_{IM}=9$ ,  $\gamma_{dM}=15$ ),  $T=5$ ,  $\lambda=1$ ,  $A_l=20$ , and  $A_d=40$ , random initial cell type assignment. 200 MCS. The constraint on vacancy nucleation is removed and a light-cell-lined, fluid-filled central cavity forms. Pattern is displayed after two MCS of  $T=0$  annealing.

cell types simply by varying the surface energies between the cells and the medium and between the cell types. We have analyzed the effect of surface energies in terms of three surface tensions, which contain all the physical information concerning the minimum-energy configuration of the cellular patterns we simulate. Our simulations allow us to explore the energy landscape, both qualitatively by displaying simulated patterns and quantitatively by measuring statistics on the topological moments of the patterns. However, the movement of a pattern on its energy surface depends on two additional parameters, the temperature and the area constraint strength. Varying the temperature or area constraint strength in the simulations reveals otherwise hidden details of the local minima of a pattern's energy surface. We have derived the following results with reference to both biological and physical patterns:

(i) For biological cell rearrangement, the observed behaviors are similar to our simulations. We therefore suggest that the energy landscape is important to biological cell sorting and that not only active cells can rearrange: slightly fluctuating or possibly even purely passive cells, lacking autonomous motile apparatus, can sort partially or totally, engulf, disperse, or form checkerboards. Thus we support either the fluctuation or fluctuationless hypotheses concerning cell migration (*F* or *S*). The additional mechanisms required by hypothesis (*A*), are not necessary to cell rearrangement, though they may be important in many biological cases.

(ii) We can distinguish spontaneous or neutral processes which have power-law time dependence from activated processes which have logarithmic time dependence. Technau and Holstein appear to have observed such logarithmic time dependence in the surface cell sorting of *hydra* aggregates, which is strong evidence for a differential adhesion mechanism: if either large fluctuations or active cell motility made the adhesion energy landscape irrelevant, the time dependencies should be either linear or power law [15].

(iii) Armstrong observed that some tissues which normally sort completely only sort partially in the presence of Cytchalasin *B* [17,25]. This incomplete sorting may be the biological analog to the freezing we observe at  $T=0$  in our model, and suggests that the energy surface for cell migration usually has at least weak local minima that trap in the absence of fluctuations, thus supporting hypothesis (*F*).

(iv) We have shown that in the case of a very high surface tension between two cell types, only active cells are able to reach the equilibrium configuration, in which the two fully sorted clusters obey the Young condition.

(v) We have explained why aggregated *hydra* cells form a monolayer but do not achieve complete sorting by comparing the time scales of these two steps (which the relative values of the heterotypic and homotypic contact energies and the area constraint strength determine).

(vi) Physically, we have investigated a phenomenon, conceptually similar to spinodal decomposition but in which finite-size effects mostly dominate. The strongest manifestations of finite size are the fixed length scale of each cell, i.e., a short-wavelength cutoff, and the limited

size of the aggregate, which implies not only a long-wavelength cutoff but also the presence of an outer medium.

(vii) The presence of the cell-Medium boundary separates complete cell sorting into two phases: a stage of monolayer formation characterized by rapid cell motion, followed by a pure bulk rearrangement characterized by logarithmic time dependence. The bulk rearrangement itself has three subphases: first a transient dominated by the short-wavelength cutoff, next a growth in length scale analogous to that of spinodal decomposition, and finally a saturation, due to the finite number of cells, which ends as a pure rounding of already formed clusters.

(viii) In addition to the previously known causes of partial sorting, we have shown that the surface tensions affect not only the dynamics at small length scales by slowing down or freezing cell-cell encounters, but also that the incompletely sorted state is the equilibrium state due to the existence of simultaneously stable light-Medium and dark-Medium interfaces.

(ix) Within our model, we have defined and simulated two phase transitions: the one at lower temperature is dynamic, and corresponds to the melting of a frozen pattern into a free pattern; the one at higher temperature is static, and corresponds to a transition between an energy and an entropy dominated equilibrium state.

Possible extensions of the model are of two major types. First, simple extensions of the existing model to three dimensions (we are currently performing such simulations), multiple cell types and larger numbers of cells. These should allow us to describe accurately simple cell-sorting examples like those of Armstrong's chicken embryo cell aggregates. Second, additions to the Hamiltonian to provide more biological realism, for example the definition of mesoglea or the introduction of time- or situation-dependent surface energies. Another possibility is to introduce additional quantum numbers to the energy term or layers to the simulation lattice, e.g., to add orientation dependence, cell polarity, or to enforce a connected, conserved cell membrane. However, such changes would reduce the analogy to other physical systems. We could also include in a simple fashion, cell growth and mitosis by varying the cells's target area and subdividing overlarge or overly oblate cells. Our goal is to describe more complex morphogenic phenomena, like cavity formation or the initiation of organ formation.

The current model suggests several biological experiments. At a fundamental level, the effective temperature of cell membrane fluctuations and the nature of the cell-cell adhesion energy need to be clarified [14]. For example, what are the changes in cell-cell adhesivity as a function of contact time? To validate our model, additional quantitative observations of the time scales of cell sorting like those of Technau and Holstein [15] (in particular, the scaling laws for correlations and boundary lengths and the relative timings of bulk sorting and monolayer formation) and of the topological moment distributions of biological tissues should allow quantitative comparisons with our analysis.

## ACKNOWLEDGMENTS

We would like to thank Professor P. B. Armstrong, Professor H. Honda, and Professor I. Takeuchi for permission to reprint figures and for supplying useful information on cell-sorting experiments. We would like to thank Professor Y. Sawada for his hospitality at Tohoku University and for helpful discussions. This research has been supported by JSPS, Monbusho, and NSF Grants No. INT 9101345 and No. DMR 9257011.

- \*Permanent address: Department of Physics, University of Notre Dame, Notre Dame, IN 46556.
- †Present address: Laboratoire de Physique Statistique, LPS-ENS, 24 rue Lhomond, 75231 Paris CEDEX 05, France.
- [1] R. Keller, *Zool. Science* **4**, 763 (1987).
  - [2] D. Fristrom, *Tissue & Cell* **20**, 645 (1988).
  - [3] R. Keller and J. Hardin, *J. Cell Sci. Suppl.* **8s**, 369 (1987).
  - [4] J. Holtfreter, *Rev. Can. Biol.* **3**, 220 (1944).
  - [5] J. Holtfreter, *J. Morph.* **80**, 25 (1947); P. Townes and J. Holtfreter, *J. Exp. Zool.* **128**, 53 (1955).
  - [6] P. Armstrong, *Crit. Rev. Biochem. Mol. Biol.* **24**, 119 (1989) (review article).
  - [7] H. Wilson, *J. Exp. Zool.* **5**, 245 (1907); M. Dan-Sohkawa, H. Yamanaka, and K. Watanabe, *J. Embryol. Exp. Morph.* **94**, 47 (1986); Y. Chun, E. Johnson, B. Gabel, and A. Cadogan, *Teratology* **27**, 81 (1983).
  - [8] K. Noda, *Zool. Mag.* **80**, 99 (1971) (in Japanese).
  - [9] A. Gierer, S. Berking, H. Bode, C. N. David, K. Flick, G. Hansmann, H. Schaller, and E. Trenkner, *Nature New Biol.* **239**, 98 (1972); K. Flick and H. Bode, in *Hydra: Research Methods*, edited by H. Lenhoff (Plenum, New York, 1983), Ch. 32.
  - [10] M. Steinberg, *Proc. Nat. Acad. Sci. USA* **48**, 1577 (1962); *Science* **137**, 762 (1962); *Proc. Nat. Acad. Sci. USA* **48**, 1769 (1962).
  - [11] M. Steinberg, *Science* **141**, 401 (1963).
  - [12] M. Steinberg, in *Cellular Membranes in Development*, edited by M. Locke (Academic, New York, 1964), p. 321; *J. Exp. Zool.* **173**, 395 (1970).
  - [13] M. Steinberg, *J. Theor. Biol.* **55**, 431 (1975). This article discusses some of the early computer simulations where each cell is represented by one site of a lattice and interacts with its neighbors: see also N. Goel *et al.*, *ibid.* **28**, 423 (1970); N. Goel and A. Leith, **28**, 469 (1970); A. Leith and N. Goel, *ibid.* **33**, 171 (1971); R. Gordon, N. Goel, M. Steinberg, and L. Wiseman, *ibid.* **37**, 43 (1972); P. Antonelli, T. Rogers, and M. Willard, *ibid.* **41**, 1 (1973). Later improvements include the long-range effects of surface tension: T. Rogers and J. Sampson, *J. Bio. Med. Comp.* **8**, 45 (1977). Simulations of other cases of cell rearrangement include: N. Goel and G. Rogers, *J. Theor. Biol.* **71**, 103 (1978); G. Rogers and N. Goel, *ibid.* **71**, 141 (1978). Studies of the topology of the cellular pattern include: R. Matela and R. Fletterick, *J. Theor. Biol.* **76**, 403 (1979); **84**, 673 (1980). Studies of molecular dynamics include: D. Greenspan, *J. Math. Biol.* **12**, 227 (1981). The simulations presented in Refs. [32] and [33] also discuss cell geometry and dynamics.
  - [14] W. Thomas and J. Yancey, *Development* **103**, 37 (1988). For a discussion of the reversibility of cell adhesion, and the existence of a true adhesion energy, see E. Evans, in *Physical Basis of Cell-Cell Adhesion*, edited by P. Bongrand (CRC, Boca Raton, 1988), Chaps. 4 and 7; D. McClay and C. Ettensohn, *A. Rev. Cell Biol.* **3**, 319 (1987).
  - [15] U. Technau and T. W. Holstein, *Developmental Biol.* **151**, 117 (1992).
  - [16] R.-M. Mege, *Médecine/Sciences* **7**, 544 (1991) (in French).
  - [17] D. McClay and C. Ettensohn, *A. Rev. Cell Biol.* **3**, 319 (1987); M. Roberson, J. Armstrong, and P. Armstrong, *J. Cell Sci.* **44**, 19 (1980).
  - [18] K. Nübler-Jung and B. Mardini, *Development* **110**, 1071 (1990).
  - [19] S. Newman and W. Comper, *Development* **110**, 1 (1990); P. B. Armstrong, *Cancer and Metastasis Rev.* **4**, 59 (1985); *Expl. Biol. Med.* **10**, 222 (1985).
  - [20] M. Takeichi, *Science* **251**, 1451 (1991).
  - [21] A. Fischer, *Médecine/Sciences* **7**, 540 (1991) (in French).
  - [22] G. Oster and A. Perelson, *J. Cell. Sci. Suppl.* **8**, 35 (1987).
  - [23] H. Phillips and G. Davis, *Am. Zool.* **18**, 81 (1978).
  - [24] F. Graner (unpublished).
  - [25] P. B. Armstrong and D. Parenti, *J. Cell. Biol.* **55**, 542 (1972); J. Overton, *Devel. Biol.* **39**, 210 (1974); **55**, 103 (1977); J. Overton and R. Kapmarski, *J. Exper. Biol.* **192**, 210 (1975); M. Steinberg and Wiseman, *J. Cell. Biol.* **55**, 606 (1972). Armstrong and Parenti specifically note that in the Cytochalasin B treated aggregates, the more cohesive dark cells apparently cannot penetrate thick barriers of less cohesive light cells.
  - [26] D'A. W. Thompson, *On Growth and Form*, 2nd ed. (Cambridge University, London, 1942); F. T. Lewis, *Anat. Rec.* **38**, 341 (1928); E. B. Matzke, *Proc. Natl. Acad. Sci. USA* **31**, 281 (1945); N. Rivier, R. Occhiali, J. Pantalone, and A. Lissowski, *J. Phys.* **45**, 49 (1984).
  - [27] J. A. Glazier, Ph.D. dissertation, University of Chicago, 1989.
  - [28] J. A. Glazier, S. P. Gross, and J. Stavans, *Phys. Rev. A* **36**, 306 (1987); J. Stavans and J. A. Glazier, *Phys. Rev. Lett.* **62**, 1318 (1990); J. Stavans, *Phys. Rev. A* **42**, 5049 (1990); J. A. Glazier, M. P. Anderson, and G. S. Grest, *Philos. Mag. B* **62**, 615 (1990); J. A. Glazier and D. Weaire, *J. Phys. Condens. Matter* **4**, 1867 (1992) (review article).
  - [29] D. Weaire, F. Bolton, P. Molho, and J. Glazier, *J. Phys. Condens. Matter* **3**, 2101 (1991).
  - [30] F. Graner and J. A. Glazier, *Phys. Rev. Lett.* **69**, 2013 (1992).
  - [31] G. Grest, D. Srolovitz, and M. Anderson, *Phys. Rev. Lett.* **52**, 1321 (1984); M. Anderson, D. Srolovitz, G. Grest, and P. Sahni, *Acta Metall.* **32**, 783 (1984); D. Srolovitz, M. Anderson, P. Sahni, and G. Grest, *ibid.* **32**, 793 (1984).
  - [32] D. Sulsky, S. Childress, and J. Perkus, *J. Theor. Biol.* **106**, 275 (1984).
  - [33] F. Graner and Y. Sawada (unpublished).
  - [34] M. Weliky and G. Oster, *Development* **109**, 373 (1990).
  - [35] E. Holm, J. Glazier, D. Srolovitz, and G. Grest, *Phys. Rev. A* **43**, 2662 (1991).
  - [36] D. Weaire and N. Rivier, *Contemp. Phys.* **25**, 59 (1984).
  - [37] H. Honda, H. Yamanaka, and G. Eguchi, *J. Embryol. Exp. Morph.* **98**, 1 (1986).
  - [38] M. Tasaka and I. Takeuchi, *J. Embryol. Exp. Morph.* **49**, 89 (1979); I. Takeuchi and M. Tasaka, *Genome* **31**, 620 (1989); I. Takeuchi, in *Cell-Cell Interactions in Early De-*

- velopment, edited by J. Gerhart (Wiley-Liss, New York, 1991), p. 249.
- [39] I. Takeuchi, T. Kakutani, and M. Tasaka, *Developmental Genetics* **9**, 607 (1988).
- [40] D. Garrod and M. Steinberg, *Nature* **244**, 568 (1973); M. Steinberg and D. Garrod, *J. Cell Sci.* **18**, 385 (1975); A. Nicol and D. Garrod, *ibid.* **38**, 249 (1979); **54**, 357 (1982).
- [41] D. A. Aboav, *Metallog.* **3**, 383 (1970); C. J. Lambert and D. Weaire, *ibid.* **14**, 307 (1981); *Philos. Mag. B* **47**, 445 (1983); N. Rivier, *ibid.* **52**, 795 (1985).
- [42] J. Jouanneau, G. C. Tucker, B. Boyer, A. M. Valles, and J. P. Thiery, *Cancer Cells* **3**, 525 (1992).
- [43] C. González Agosti, Diplomarbeit, Universität Zurich, 1985 (unpublished). (Video recordings of cell engulfment are available from C. González Agosti.)
- [44] P. Armstrong and M. Armstrong, *J. Cell. Sci.* **69**, 179 (1984).
- [45] L. Graf and A. Gierer, *Wilhelm Roux Arch. Devl. Biol.* **188**, 141 (1980).
- [46] X. Zhang and M. Sarras (unpublished); M. Sarras (private communication).
- [47] S. Fraser, C. Green, H. Bode, and N. Gilula, *Science* **237**, 49 (1987).

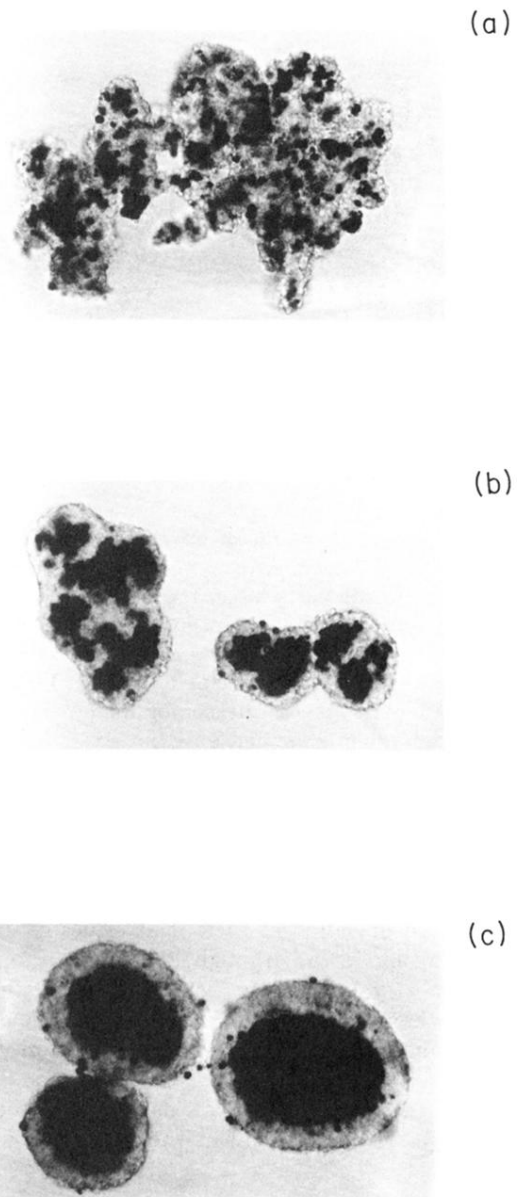


FIG. 10. Cell sorting. Observations by Armstrong of cell sorting between pigmented (dark) and neural (light) retinal cells in seventh-day chick embryo in three-dimensional suspended aggregates. Reprinted with permission from P. Armstrong, Crit. Rev. Biochem. and Mol. Biol. **24**, 119 (1989). Copyright CRC Press, Inc., Boca Raton, FL. (a) Random mixing at 5 h. (b) Partial cell sorting at 19 h. (c) Complete cell sorting at 48 h. Armstrong notes that the detached dark cells in (b) and (c) are dead. Pictures show two-dimensional sections of three-dimensional aggregates.

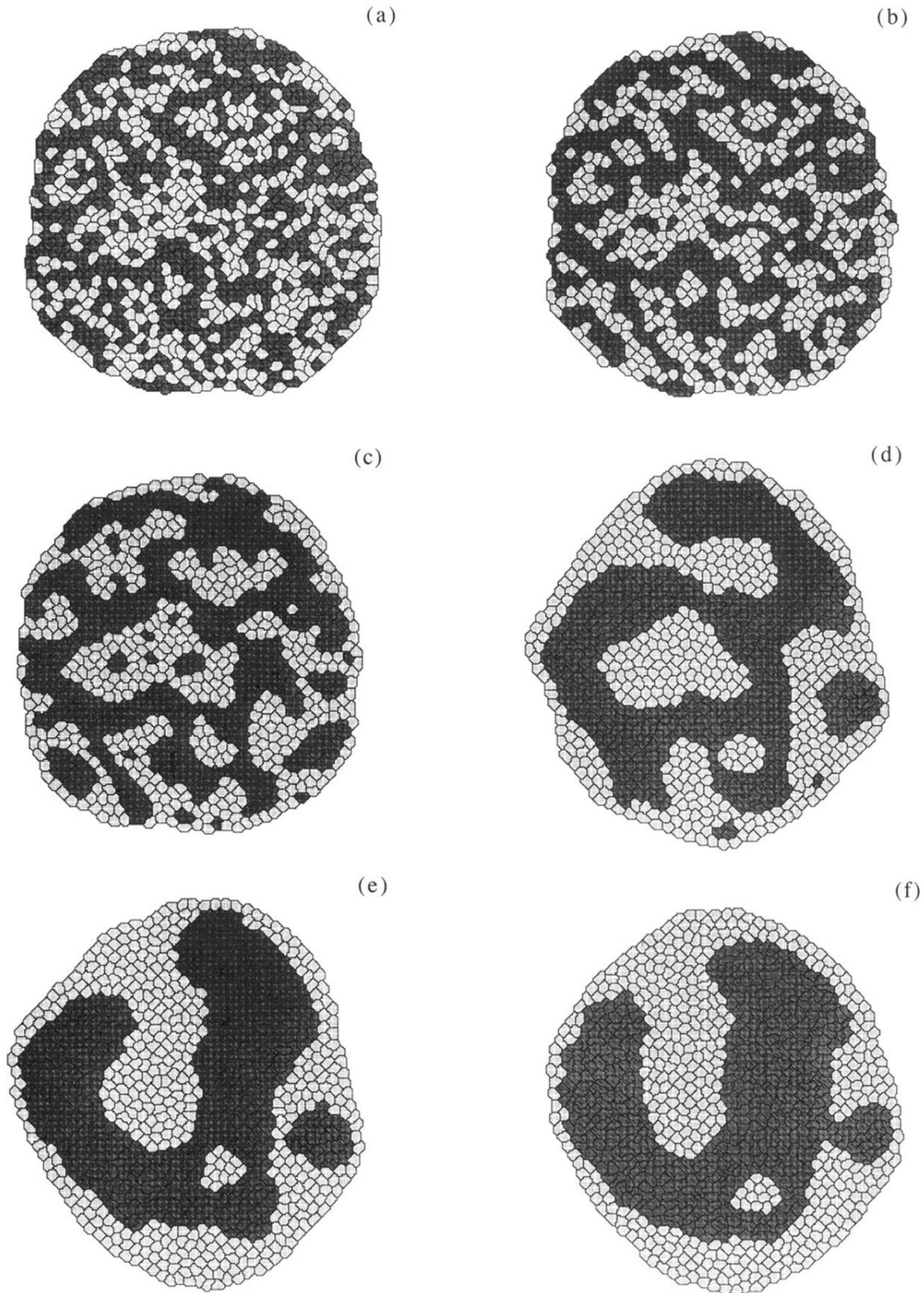
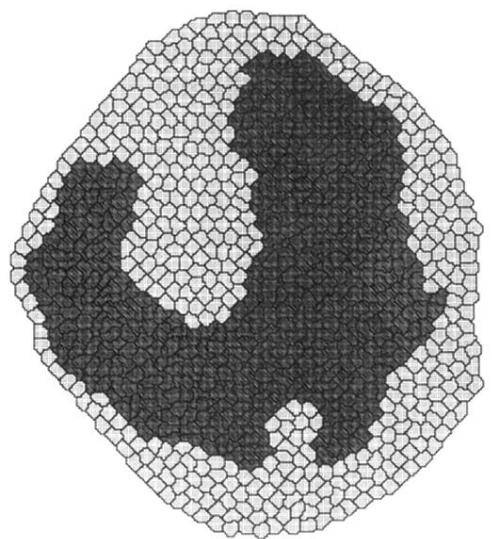


FIG. 12. Cell sorting. Simulation.  $J_{ll} = 14$ ,  $J_{dd} = 2$ ,  $J_{ld} = 11$ ,  $J_{lM} = J_{dM} = 16$  (yielding  $\gamma_{ld} = 3$ ,  $\gamma_{lM} = 9$ ,  $\gamma_{dM} = 15$ ),  $T = 10$ , and  $\lambda = 1$ , random initial cell type assignment. (a) 0 MCS. (b) 10 MCS. (c) 100 MCS. (d) 1000 MCS. (e) 3000 MCS. (f) 4000 MCS. (g) 5000 MCS. (h) 13 500 MCS. Patterns are displayed after two MCS of  $T = 0$  annealing.

(g)



(h)

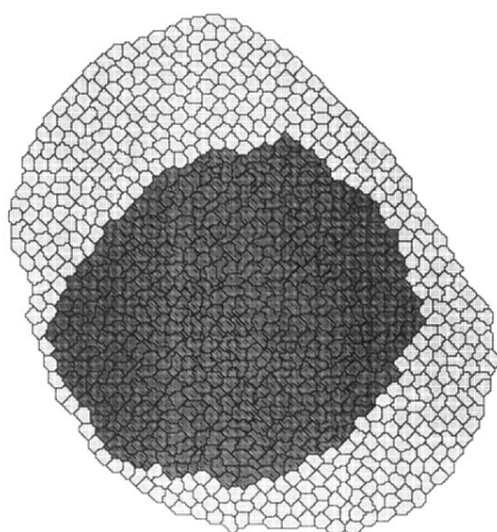


FIG. 12. (*Continued*).

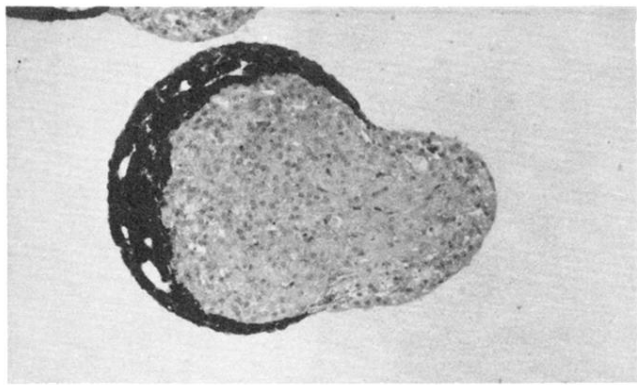


FIG. 17. Engulfment. Observation by Armstrong of cell engulfment of heat cells (light) by pigmented retinal cells (dark) from tenth-day chicken embryo in three-dimensional suspended aggregates. Reprinted with permission from P. Armstrong, Crit. Rev. Biochem. and Mol. Biol. **24**, 119 (1989). Copyright CRC Press, Inc., Boca Raton, FL. Figure shows a two-dimensional section of a three-dimensional culture after 48 h.

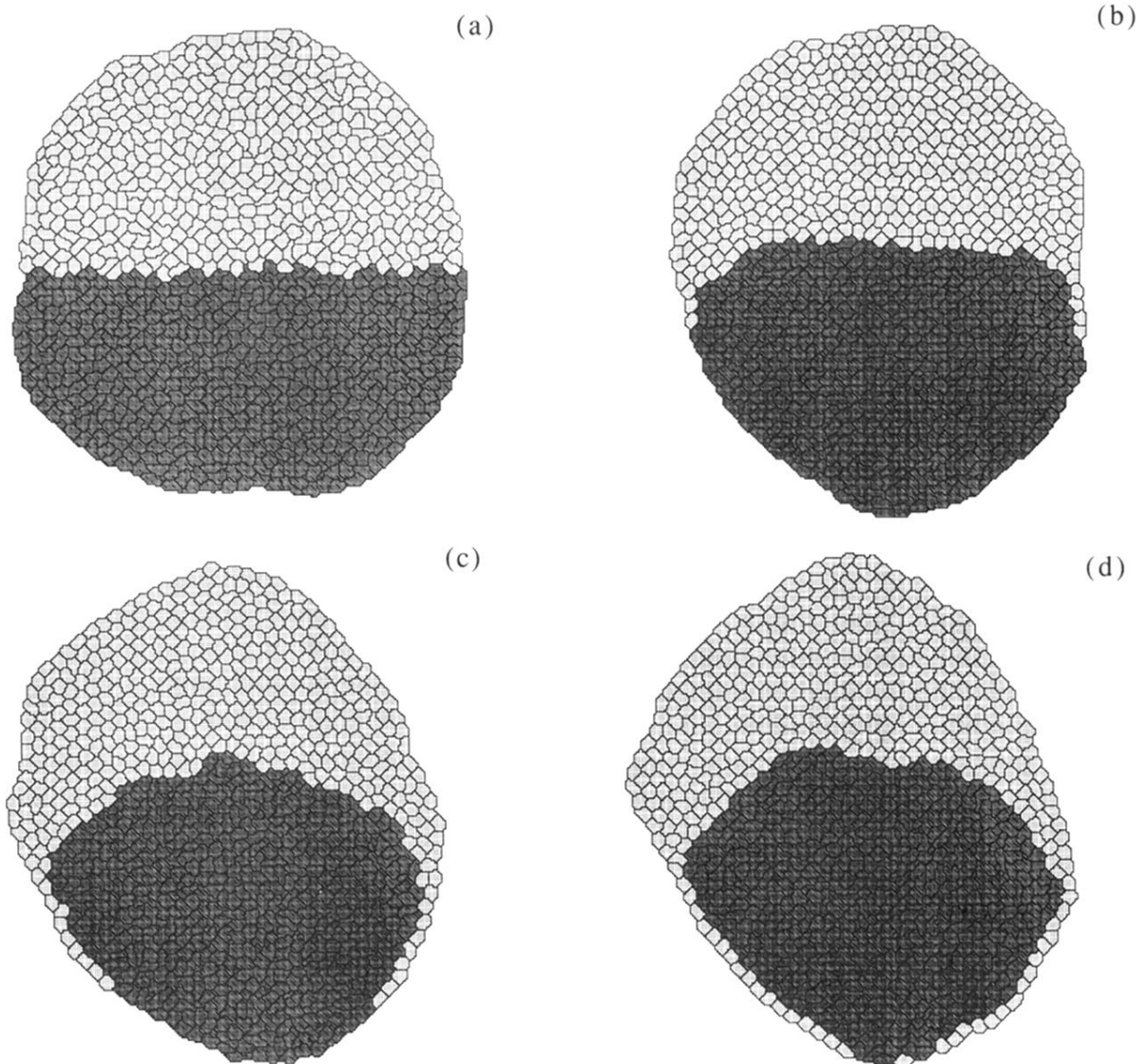


FIG. 18. Engulfment. Simulation.  $J_{ll} = 14$ ,  $J_{dd} = 2$ ,  $J_{ld} = 11$ ,  $J_{lM} = J_{dM} = 16$  (yielding  $\gamma_{ld} = 3$ ,  $\gamma_{lM} = 9$ ,  $\gamma_{dM} = 15$ ), and  $\lambda = 1$ , initial cell type assignment upper half light, lower half dark. (a) Initial condition, 0 MCS. (b) 1000 MCS. (c) 5000 MCS. (d) 10 000 MCS.  $\langle n \rangle = 6.14 \pm 0.03$ ,  $\mu_2 = 0.76 \pm 0.06$ ,  $\mu_3 = 0.39 \pm 0.15$ ,  $\mu_4 = 2.81 \pm 0.74$ . Patterns are displayed after two MCS of  $T = 0$  annealing.

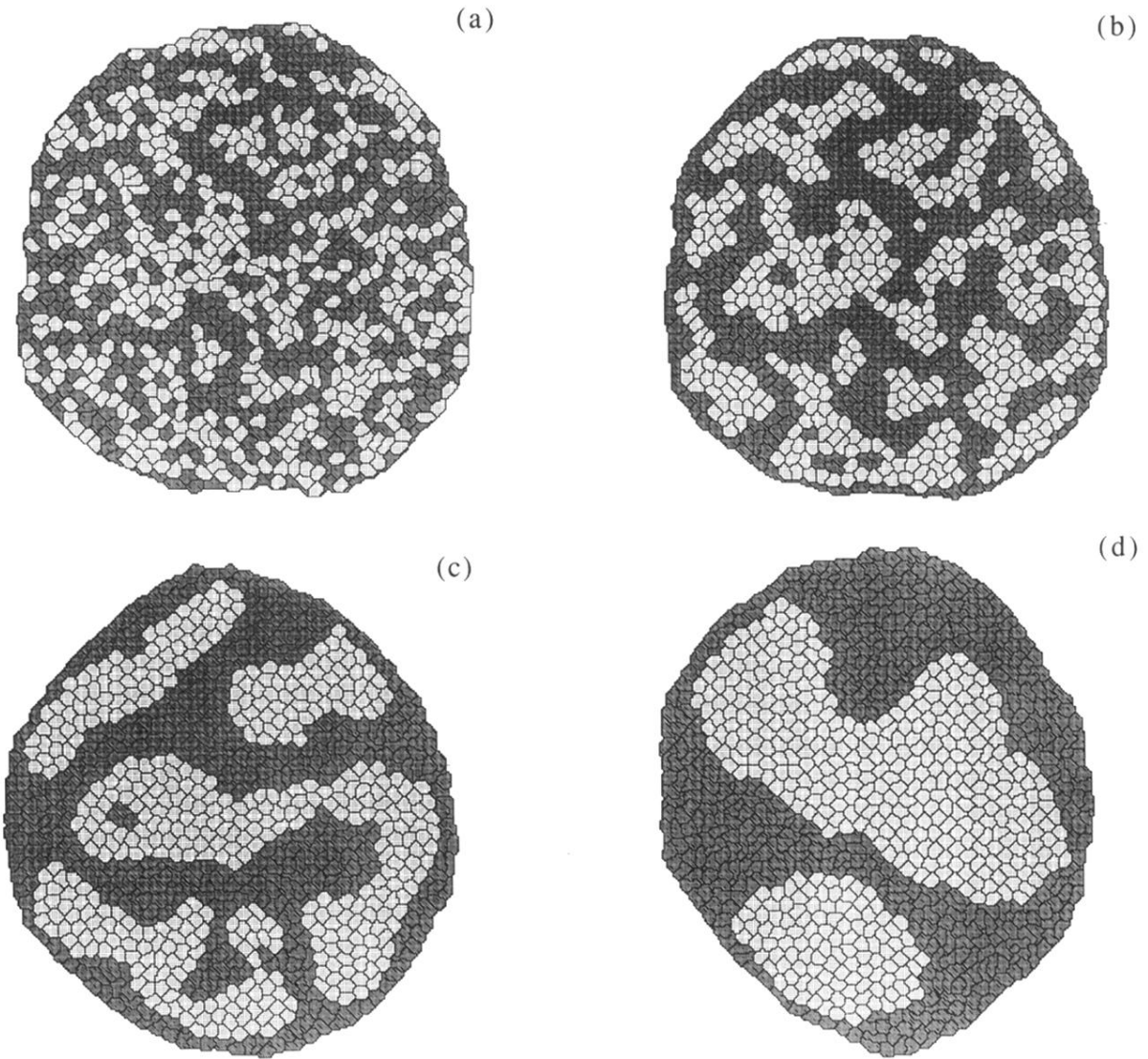


FIG. 20. Position reversal. Simulation.  $J_{ll} = 14$ ,  $J_{lM} = 30$ ,  $J_{dd} = 2$ ,  $J_{dM} = 16$ ,  $J_{ld} = 11$  (yielding  $\gamma_{ld} = 3$ ,  $\gamma_{lM} = 23$ ,  $\gamma_{dM} = 15$ ),  $T = 10$ , and  $\lambda = 1$ , random initial cell type assignment. (a) Initial condition, 0 MCS. (b) 50 MCS. (c) 5000 MCS. (d) 5000 MCS.  $\langle n \rangle = 6.08 \pm 0.03$ ,  $\mu_2 = 0.71 \pm 0.06$ ,  $\mu_3 = 0.24 \pm 0.14$ ,  $\mu_4 = 2.40 \pm 0.65$ . Patterns are displayed after two MCS of  $T = 0$  annealing.

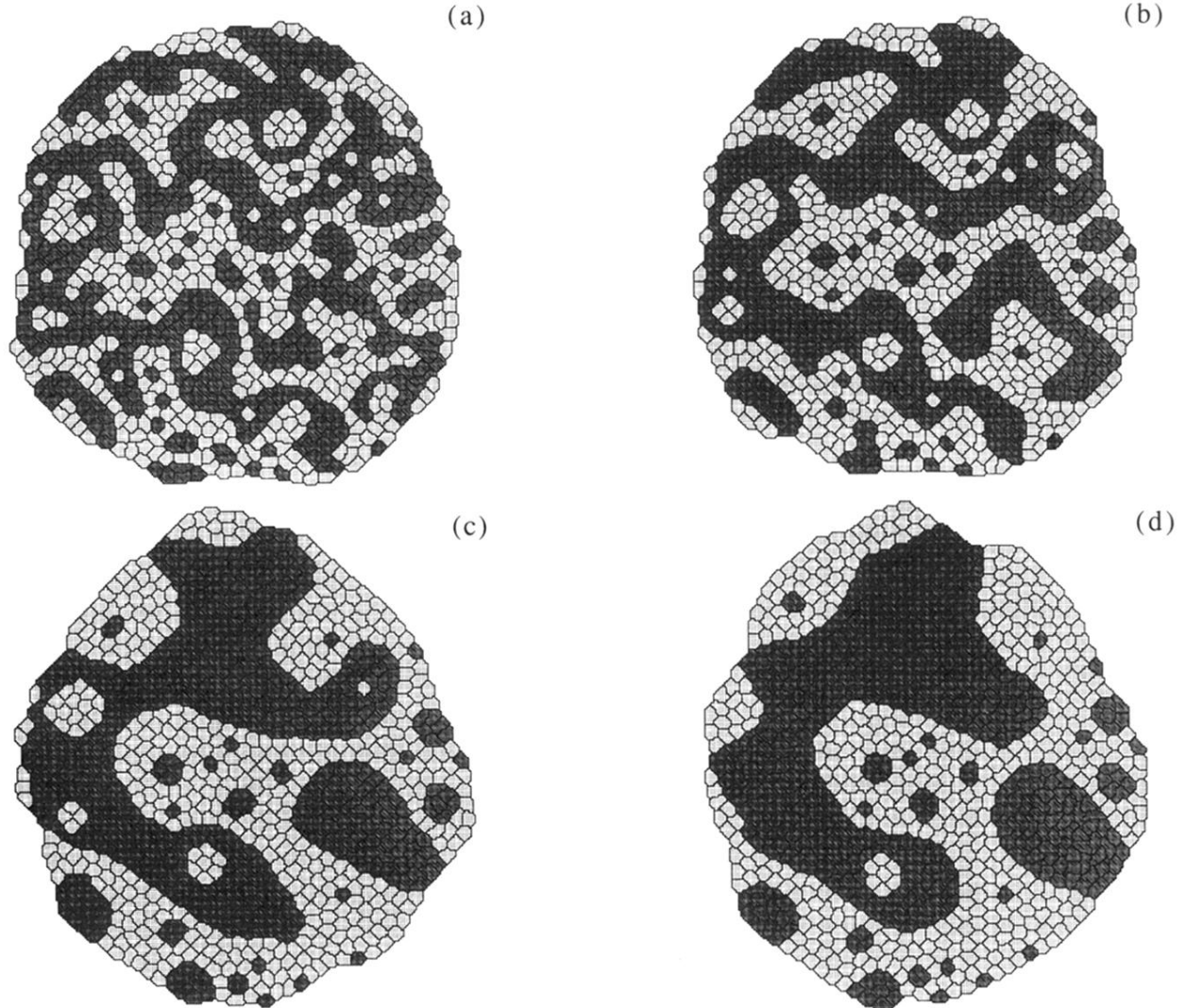


FIG. 22. Partial cell sorting. Simulation.  $J_{ll} = 11$ ,  $J_{dd} = 2$ ,  $J_{ld} = 14$ ,  $J_{lM} = J_{dM} = 16$  (yielding  $\gamma_{ld} = 7.5$ ,  $\gamma_{lM} = 10.5$ ,  $\gamma_{dM} = 15$ ),  $T = 5$ ,  $\lambda = 1$ , random initial cell type assignment. (a) 10 MCS, (b) 100 MCS, (c) 1000 MCS, (d) 2000 MCS. Patterns are displayed after two MCS of  $T = 0$  annealing.

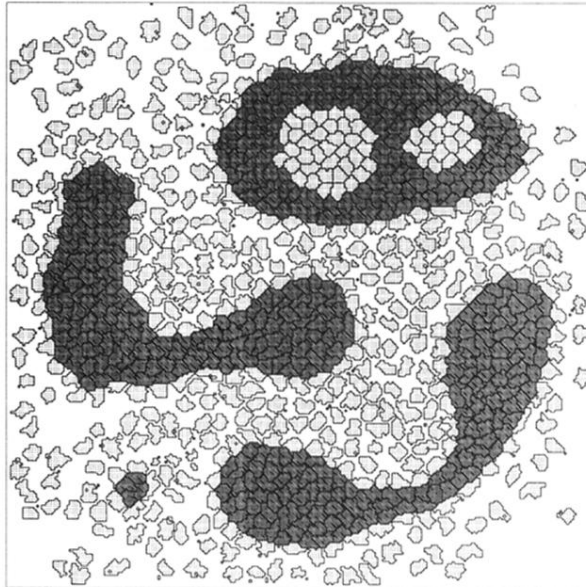


FIG. 25. Cell dispersal. Simulation.  $J_{II} = 14$ ,  $J_{dd} = 4$ ,  $J_{ld} = 11$ ,  $J_{IM} = 2$ ,  $J_{dM} = 16$  (yielding  $\gamma_{ld} = 2$ ,  $\gamma_{IM} = -5$ ,  $\gamma_{dM} = 14$ ),  $T = 5$ , and  $\lambda = 1$ , random initial cell type assignment. 480 MCS. Dark cells remain compact and round, light cells in contact with the medium disperse. Displayed pattern is unannealed.

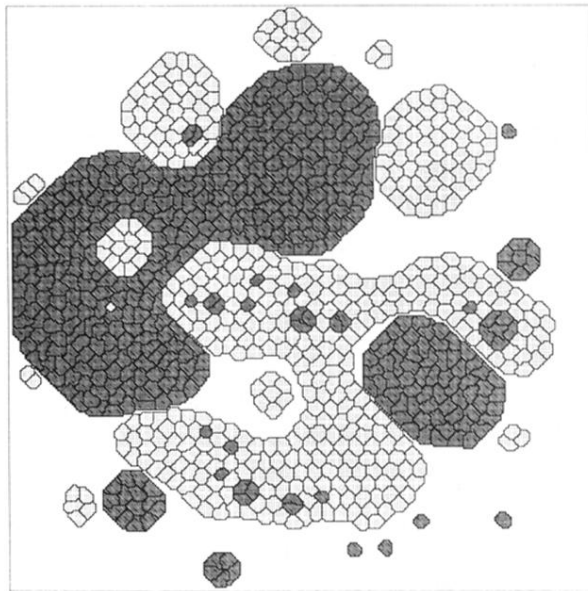


FIG. 26. Cell dispersal. Simulation.  $J_{ll}=14$ ,  $J_{dd}=2$ ,  $J_{ld}=35$ ,  $J_{lM}=J_{dM}=16$  (yielding  $\gamma_{ld}=27$ ,  $\gamma_{lM}=9$ ,  $\gamma_{dM}=15$ ),  $T=5$ , and  $\lambda=1$ , random initial cell type assignment. 2000 MCS. Both light and dark cells remain compact and round, but the clusters separate. A few isolated dark cells also occur. Pattern is displayed after two MCS of  $T=0$  annealing.

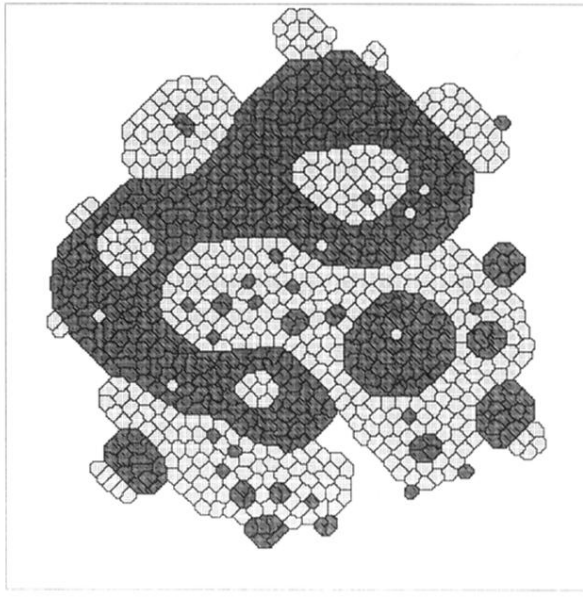


FIG. 27. Cell dispersal. Simulation.  $J_{ll}=14$ ,  $J_{dd}=2$ ,  $J_{ld}=29$ ,  $J_{lM}=J_{dM}=16$  (yielding  $\gamma_{ld}=21$ ,  $\gamma_{lM}=9$ ,  $\gamma_{dM}=15$ ),  $T=5$ , and  $\lambda=1$ , random initial cell type assignment. 2000 MCS. Both light and dark cells remain compact and round, clusters do not separate. The result is an extreme case of partial cell sorting. Pattern is displayed after two MCS of  $T=0$  annealing.

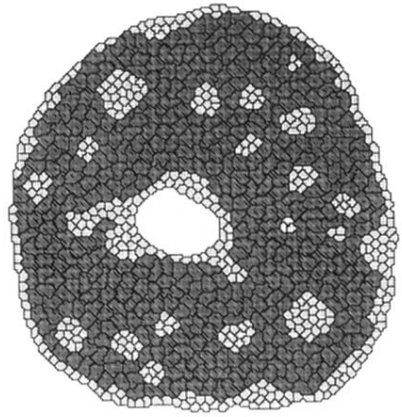


FIG. 28. Vacancy nucleation. Simulation.  $J_{ll}=14$ ,  $J_{dd}=2$ ,  $J_{ld}=11$ ,  $J_{lM}=J_{dM}=16$  (yielding  $\gamma_{ld}=3$ ,  $\gamma_{lM}=9$ ,  $\gamma_{dM}=15$ ),  $T=5$ ,  $\lambda=1$ ,  $A_l=20$ , and  $A_d=40$ , random initial cell type assignment. 200 MCS. The constraint on vacancy nucleation is removed and a light-cell-lined, fluid-filled central cavity forms. Pattern is displayed after two MCS of  $T=0$  annealing.

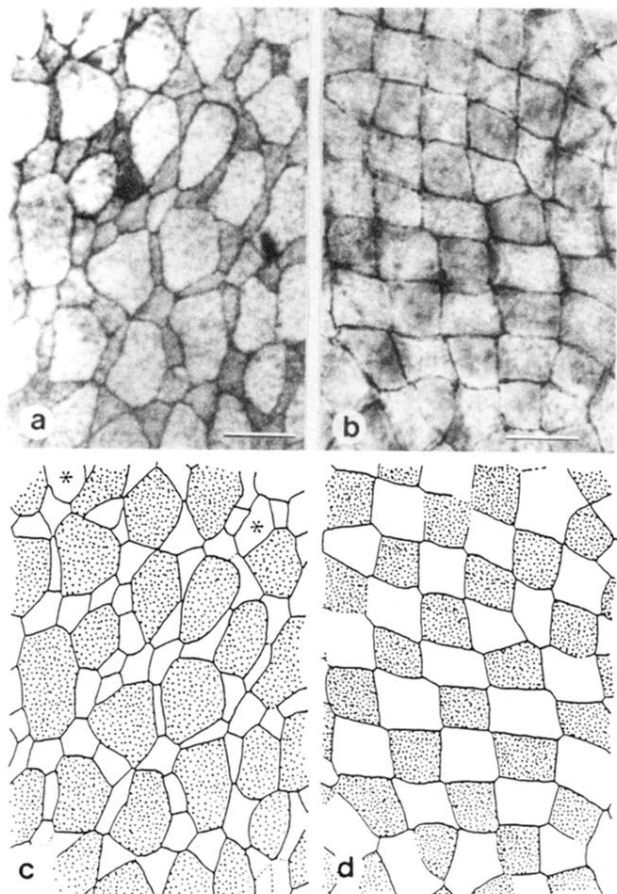


FIG. 6. Checkerboard. Japanese quail oviduct epithelium, photographed by Honda, Yamanaka, and Eguchi, reprinted with permission from H. Honda, H. Yamanaka, and G. Eguchi, *J. Embryol. Exp. Morph.* **98**, 1 (1986). Copyright Company of Biologists, Ltd., Cambridge, England. (a) and (c) Immature oviduct. (b) and (d) Mature oviduct after the division of each ciliated (dark) cell.

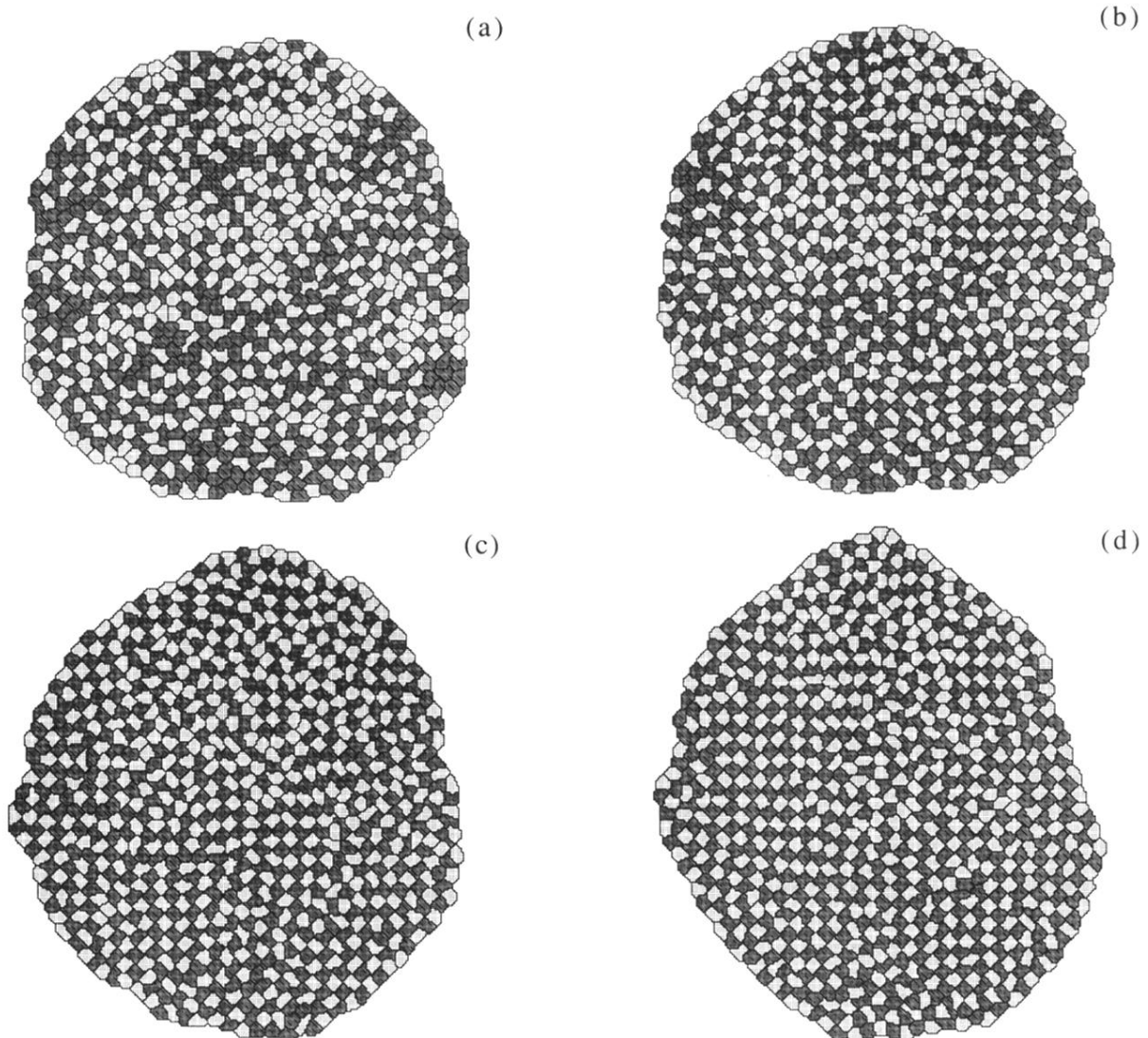


FIG. 7. Checkerboard. Simulation.  $J_{ll} = 10$ ,  $J_{dd} = 8$ ,  $J_{ld} = 6$ ,  $J_{lM} = J_{dM} = 12$  (yielding  $\gamma_{ld} = -3$ ,  $\gamma_{lM} = 7$ ,  $\gamma_{dM} = 8$ ),  $T = 10$ , and  $\lambda = 1$ , random initial cell type assignment. (a) 10 MCS, (b) 100 MCS, (c) 1000 MCS, (d) 2000 MCS. Patterns are displayed after two MCS of  $T = 0$  annealing.